

1 Porosity evolution of mafic crystal mush during 2 reactive flow

3 Matthew L. M. Gleeson^{1,2}, C. Johan Lissenberg¹, and Paula M. Antoshechkina³

4 ¹School of Earth and Environmental Sciences, Cardiff University, Main Building, Park Place, CF10 3AT,
5 UK.

6 ²Department of Earth and Planetary Science, University of California Berkeley, McCone Hall, Berkeley,
7 CA, USA

8 ³Division of Geological and Planetary Sciences, Caltech, Pasadena, CA, 91125, USA

9 ABSTRACT

10 **The emergence of the “mush paradigm” has raised several questions for conventional models of**
11 **magma storage and extraction: how are melts extracted to form eruptible liquid-rich domains?**
12 **What mechanism controls melt transport in mush-rich systems? Recently, reactive flow has been**
13 **proposed as a major contributing factor in the formation of high porosity, melt-rich regions. Yet,**
14 **owing to the absence of accurate geochemical simulations, the influence of reactive flow on the**
15 **porosity of natural mush systems remains under-constrained. Here, we use a thermodynamically**
16 **constrained model of melt-mush reaction to simulate the chemical, mineralogical, and physical**
17 **consequences of reactive flow in a multi-component mush system. Our results demonstrate that**
18 **reactive flow within troctolitic to gabbroic mushes can drive large changes in mush porosity. For**
19 **example, primitive magma recharge drives an increase in the system porosity and could trigger melt**
20 **channelization or mush destabilization, aiding rapid melt transfer through low-porosity mush**
21 **reservoirs.**

22 MAIN

23 For most of the last century, models of igneous differentiation and crustal magma transport have been
24 dominated by the hypothesized presence of large, melt-rich magma chambers¹⁻⁴. Within the last few
25 decades, however, there has been a paradigm shift in how magmatic systems are pictured, moving
26 away from the magma chamber hypothesis and towards a model in which magma reservoirs are
27 dominated by crystal-rich mush⁵⁻¹⁰.

28 The importance of mush-dominated magma reservoirs was first recognized at mid-ocean ridges,
29 where geophysical surveys failed to identify the presence of large, melt-rich magma chambers^{11,12},
30 and petrological analyses revealed chemical variations that cannot easily be explained by
31 crystallisation in large, well-mixed magma chambers¹³⁻¹⁵. Petrological and geochemical observations
32 of erupted volcanic products and their cumulate counterparts, from both ocean island and arc volcanic

33 systems, has since confirmed the importance of mush-dominated storage regions worldwide^{16–22}. The
34 absence of geophysical evidence for melt-rich magmatic systems (i.e., > 50% melt) in the upper crust
35 beneath active volcanic regions continues to support the mush paradigm^{23,24}, although the limitations
36 of seismic tomography for imaging thin (<200 m thick) melt-rich bodies has recently been
37 highlighted.²⁵

38 The mush paradigm raises fundamental questions about melt transport: if magma plumbing systems
39 are dominated by crystal mush, how is melt transported through them? How does melt accumulate
40 to form eruptible reservoirs? Models for melt extraction or accumulation in mush-dominated systems
41 have traditionally focused on the role of melt buoyancy and crystal compaction, squeezing the more
42 buoyant magma out of the crystalline mush^{26–29}. Evidence for crystal compaction is found in the form
43 of plastic deformation of crystals from various magmatic systems worldwide that are shown to have
44 large, long-lived mush reservoirs^{17,30}; however, it remains unclear whether magma extraction and the
45 solidification of mush systems can be driven by compaction alone^{31,32}. As a result, attention has turned
46 towards the influence of reactive flow, where a melt percolating through a porous crystal framework,
47 possibly aided by mush compaction, reacts with the surrounding crystals ('reactive flow' is here used
48 as a general term to describe both reactive porous flow along grain boundaries and focused flow in
49 melt channels generated by reactive processes)^{10,30,33}. Existing numerical models suggest that this
50 process can generate melt-rich domains, channels or layers within crustal mush systems, and that
51 reactive flow may be the dominant mechanism of melt transport and melt extraction in mush-
52 dominated magmatic reservoirs^{33,34}. However, current numerical models incorporate highly simplistic
53 empirical chemical parameterizations involving only a single solid composition, which may not
54 accurately recreate the complexity of natural, mineralogically diverse magmatic systems. The
55 influence of reactive flow on the chemical and physical signature in gabbroic, troctolitic, and wehrlitic
56 mush systems has also been investigated through petrological analysis combined with assimilation-
57 fractional crystallization (AFC) calculations^{35–37}. However, as AFC calculations are not energy-
58 constrained, they likely violate the conservation of energy principle that governs the behaviour of
59 natural systems (e.g., through the use of thermodynamically infeasible assimilated to crystallised mass
60 ratios – M_a/M_c). As a result, the feasibility of reactive flow as a melt transport mechanism remains to
61 be established, and our understanding of its influence on melt accumulation remains limited.

62 Here, we examine the influence of reactive flow on the porosity of troctolitic to gabbroic mush
63 systems, relevant to mid-ocean ridge magmatism, using thermodynamic simulations implemented
64 through alphaMELTS for MATLAB³⁸ (rhyolite-MELTS v1.0.2) that capture the full chemical complexity
65 and phase equilibria of natural systems. In addition, by using a Bayesian approach to examine key
66 input parameters (e.g., temperature, initial porosity), we can consider the influence of different

67 variables on the porosity evolution of mafic mushes. This approach also allows us to examine the role
68 of kinetic factors during melt-mush reaction, such as variable mineral dissolution rates^{39,40}, which
69 might influence the mineralogy of the reacted solid assemblage. Our model results reveal that the
70 influence of reactive flow on the porosity evolution of mafic mush systems beneath active spreading
71 centres is dominantly controlled by the phase proportions in the reacted solid material. In addition,
72 our models highlight key conditions that might drive an increase in the system porosity, triggering
73 mush fluidization or the formation of melt channels, as well as situations where reactive flow causes
74 a decrease in the system porosity, limiting future melt transport and likely driving the extreme
75 chemical enrichment observed in magmatic cumulates^{18,41,42}. The thermodynamic approach used here
76 confirms that simple chemical parameterisations used in recent numerical models of reactive flow are
77 insufficient to capture the complex behaviour of natural magmatic systems³³ and highlight that
78 reactive porous flow could be key to melt transport within magmatic mush zones. Overall, our results
79 have substantial implications for the dynamics of magmatic systems in the build-up to volcanic
80 eruptions.

81 RESULTS

82 A THERMODYNAMIC APPROACH TO MELT-MUSH REACTION

83 Geochemical and textural signatures of reactive flow have been observed in mafic cumulate rocks
84 from a wide range of tectonic settings worldwide, including mid-ocean ridge^{36,41,43}, ocean island¹⁸, and
85 arc volcanic systems²². However, current chemical and dynamical models of this process lack the
86 ability to accurately determine how reactive flow in a heterogeneous crystal framework influences the
87 porosity of a mush, which hampers our understanding of the implications of reactive flow for the
88 efficiency of melt transport. To address this problem, we simulate the interaction of basaltic melts
89 with olivine + plagioclase \pm clinopyroxene mush systems in a series of dissolution-reprecipitation
90 reactions using alphaMELTS for MATLAB (rhyolite-MELTS v1.0.2)^{44,45}. The flexibility of our new model
91 enables us to examine the influence of key parameters on mush porosity evolution, including the
92 composition and mineralogy of the initial crystal-framework and the reacted assemblage, as well as
93 the initial porosity and temperature of the system. Our work uses mid-ocean ridge magmatic systems
94 as a template, as the influence of reactive porous flow has been well-documented in these systems,
95 providing a wealth of data to compare to our models^{36,37,41,42}. In addition, mid-ocean ridge magmatic
96 systems are typically water-poor and hydrous minerals such as amphibole or biotite are rare, thus

97 minimizing errors resulting from the absence of accurate thermodynamic data in the MELTS models
 98 for these hydrous phases.

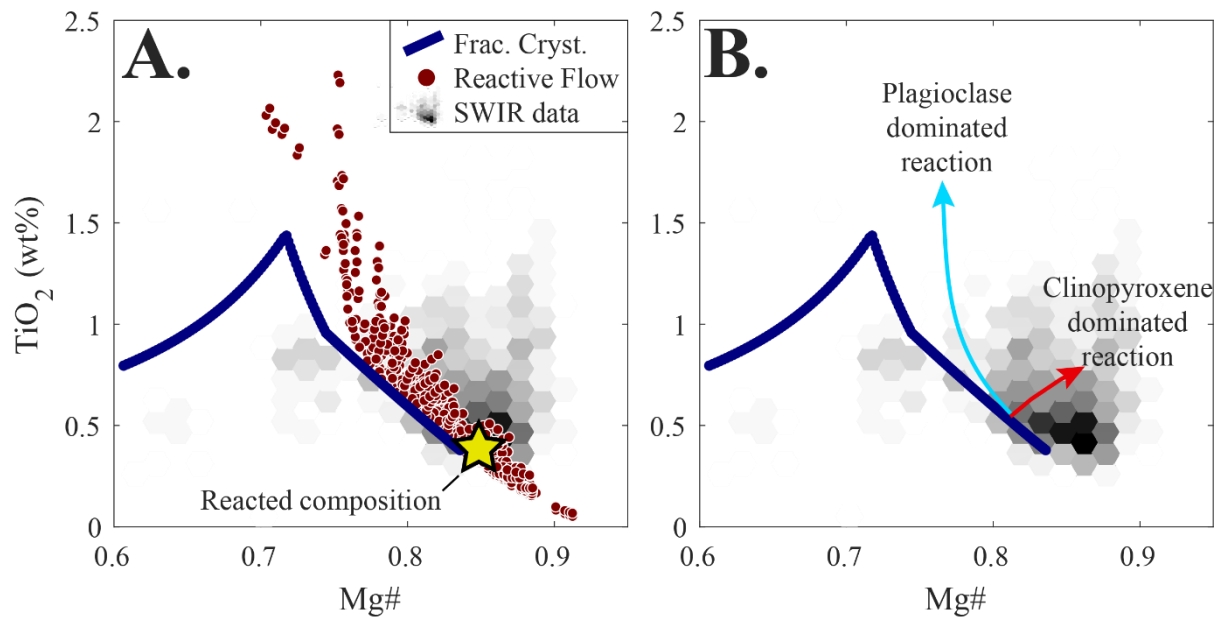


Figure 1 – Consequences of reactive flow on clinopyroxene compositions. Fractional crystallisation models, using an initial melt composition based on primitive basalts from the Southwest Indian Ridge (see Methods), predict clinopyroxene compositions that bracket the lower TiO₂ contents observed in natural mid-ocean ridge gabbros (data from ref.³⁶). Reactive flow models were run over a range of temperatures (1150–1230°C) with other parameters equivalent to those used in Scenarios 1 and 2 (see Methods and Supplementary Information). **A.** TiO₂ enrichment is observed in many modelled clinopyroxenes, consistent with the natural data. In addition, reactive flow can also cause crystallisation of high Mg# (>0.90) clinopyroxenes – higher than any values observed in crystallisation models or experimental data⁵⁶, but in line with the natural data. **B.** Schematic representation of the different paths followed by models dominated by plagioclase and clinopyroxene dissolution.

99 Initially, to determine whether our models provide an accurate simulation of natural mush processes,
 100 we create 200 reactive flow paths over a range of temperatures (1150 – 1230°C), where a basaltic
 101 melt phase reacts with a gabbroic mush zone, and track key chemical parameters over six melt-mush
 102 reaction cycles. Results demonstrate that signatures linked to reactive flow in mid-ocean ridge settings
 103 are recreated by our models. These include the anomalously high TiO₂ signature and high Mg# (>90)
 104 of gabbroic clinopyroxenes, which cannot be generated by fractional crystallisation models alone yet
 105 are frequently observed in the rock record^{30,36,46} (Fig. 1). Consequently, our energy-constrained
 106 reactive flow models, which require far fewer assumptions than traditional Assimilation-Fractional
 107 Crystallization calculations^{35,36}, provide a meaningful simulation of the chemical reactions that occur
 108 in natural magmatic mush systems. As such, we can use these models to assess the influence of
 109 reactive flow on the porosity evolution of magmatic systems. To do so, we track the Melt Mass Ratio

110 $(M_{Final}^{Melt} / M_{Initial}^{Melt})$ of the local chemical system through the reaction.

111 We consider three scenarios that are appropriate to reactive flow within mid-ocean ridge magma
112 reservoirs. First, we simulate the interaction of a cotectic, three-phase
113 (olivine+plagioclase+clinopyroxene) saturated basaltic melt, which lies along the trend defined by
114 fractional crystallization of a mantle-derived parental magma, with a gabbroic mush (Ol₅:Plag₅₅:Cpx₄₀).
115 A second scenario considers higher temperature simulations, where the initial melt phase is only
116 saturated in olivine and plagioclase (i.e., undersaturated with respect to clinopyroxene), but all other
117 parameters are equivalent to those used in scenario 1. Finally, we consider infiltration of 2-or-3 phase
118 saturated basaltic melts into a troctolitic mush system (Ol₂₅:Plag₇₀:Cpx₅) over a range of temperatures
119 (1150 – 1230°C).

120 In each simulation, the initial porosity and temperature of the mush and the melt/solid ratio (defined
121 by setting the mass of reacted, or assimilated, solid material relative to the mass of melt) are randomly
122 selected from a uniform distribution to test their influence on the model results (see Supplementary
123 Information). In addition, by considering the mineralogy of the dissolved solid assemblage separately
124 to the mineralogy of the mush system we can evaluate the role of varying dissolution rates or mineral
125 stability. Additionally, our different scenarios allow the importance of phase saturation in the liquid
126 component to be evaluated.

127 There is abundant evidence in natural magmatic systems that reactive flow proceeds via dissolution-
128 reprecipitation reactions as modelled here^{37,41,43}. However, the exact parameters of these reactions,
129 for example, how much dissolution occurs before precipitation is triggered, remain unclear. By
130 considering this problem using a Bayesian approach to sample a broad parameter space for variables
131 such as the mass of reacted material at each step, we can determine the sensitivity of reactive flow to
132 these critical yet under-constrained parameters.

133 REACTIVE CONTROLS ON MUSH POROSITY

134 450 simulations were run for each of the three scenarios. These simulations reveal that during
135 infiltration of three-phase saturated basalts into a gabbroic mush system (i.e., Scenario 1), the modal
136 proportion of clinopyroxene, relative to plagioclase increases in the mush, consistent with reactions
137 proposed based on observations of natural systems³⁰ and thus further supporting the validity of our
138 models (see Supplementary Information). In fact, many models with low proportions of plagioclase in
139 the reacted solid assemblage ($X_{reaction}^{Plagioclase} < 0.2$) in all three scenarios predict that the dissolved solid
140 material shifts the local chemical systems far enough from the olivine-plagioclase-clinopyroxene
141 cotectic that no plagioclase crystallisation is predicted (Supplementary Information). Nevertheless,

142 there is generally a strong correlation between the proportion of a given mineral in the reacted solid
 143 assemblage and the proportion of that phase in the crystallised component (Fig. 2).

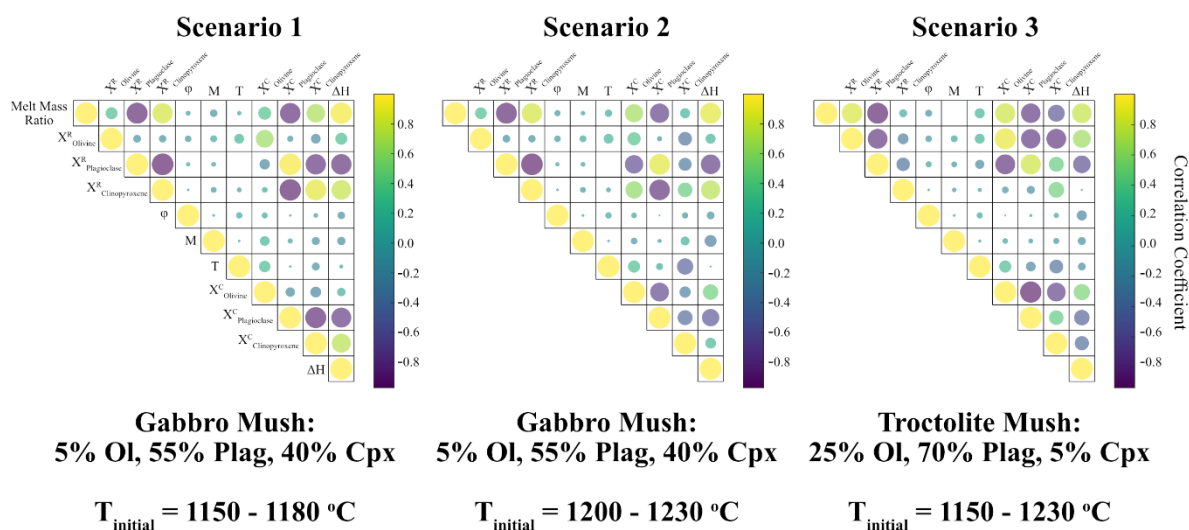


Figure 2 – Correlation matrices for each scenario. In all models there is a strong correlation between the Melt Mass Ratio, the proportion of plagioclase in the dissolved/reacted solid assemblage ($X_{\text{Plagioclase}}^R$), and the change of specific enthalpy in the melt phase (ΔH : defined as the difference between the specific enthalpy of the melt phase prior to, and after melt-mush reaction). There are, however, subtle differences between the scenarios. For example, in scenario 2, there is a weaker correlation between the proportion of clinopyroxene in the crystallised assemblage ($X_{\text{Clinopyroxene}}^C$) and the Melt Mass Ratio than there is in scenario 1. This is likely due to the higher temperature of the scenario 2 models and the clinopyroxene-undersaturated nature of the initial melt phase (and thus lower contribution of clinopyroxene to the crystallising assemblage).

144 We further note that, for the parameters chosen in this study, the Melt Mass Ratio of reaction is
 145 typically centred around 0.95 - 1 (Fig. 3). In fact, when the randomly selected dissolved solid
 146 assemblage (see Methods) approximates the mineralogy of the mush system, the Melt Mass Ratio is
 147 consistently between 0.9 and 1.05. As a result, unless other factors drive the preferential dissolution
 148 of one phase relative to the others, which could occur due to differing dissolution rates and/or
 149 variations in the melt saturation state, reactive flow often has little to no influence on the porosity of
 150 mush systems: dissolution and reprecipitation are close to equal, and reactive flow proceeds by a
 151 process akin to zone refining^{47,48}. While this result is dependent on other variables, as explored in more
 152 detail below, it indicates that reactive flow may operate ‘freely’, continually working to transport melt
 153 through magmatic mush systems and enabling chemical modification of the melt and crystal phases
 154 due to the ongoing reactions. However, while the mean Melt Mass Ratio in all scenarios is ~ 1 , the total
 155 range of values observed extends from ~ 0.7 to ~ 1.3 , indicating that under certain conditions, reactive
 156 flow can have substantial impacts on mush porosity and thus the efficiency of melt transport.

157 Consideration of all simulations in each scenario reveals that variations in mush temperature, initial
 158 porosity, and the solid/melt ratio of the reaction have little influence on the Melt Mass Ratio of

159 reaction (Fig. 2). Instead, our simulations indicate that the mineralogy of the dissolved solid
 160 assemblage, here treated independently from the mineralogy of the mush to account for kinetic
 161 factors such as variations in mineral dissolution rates⁴⁹, represents the dominant control on porosity
 162 changes within mush systems. In natural systems, the temperature and melt composition may

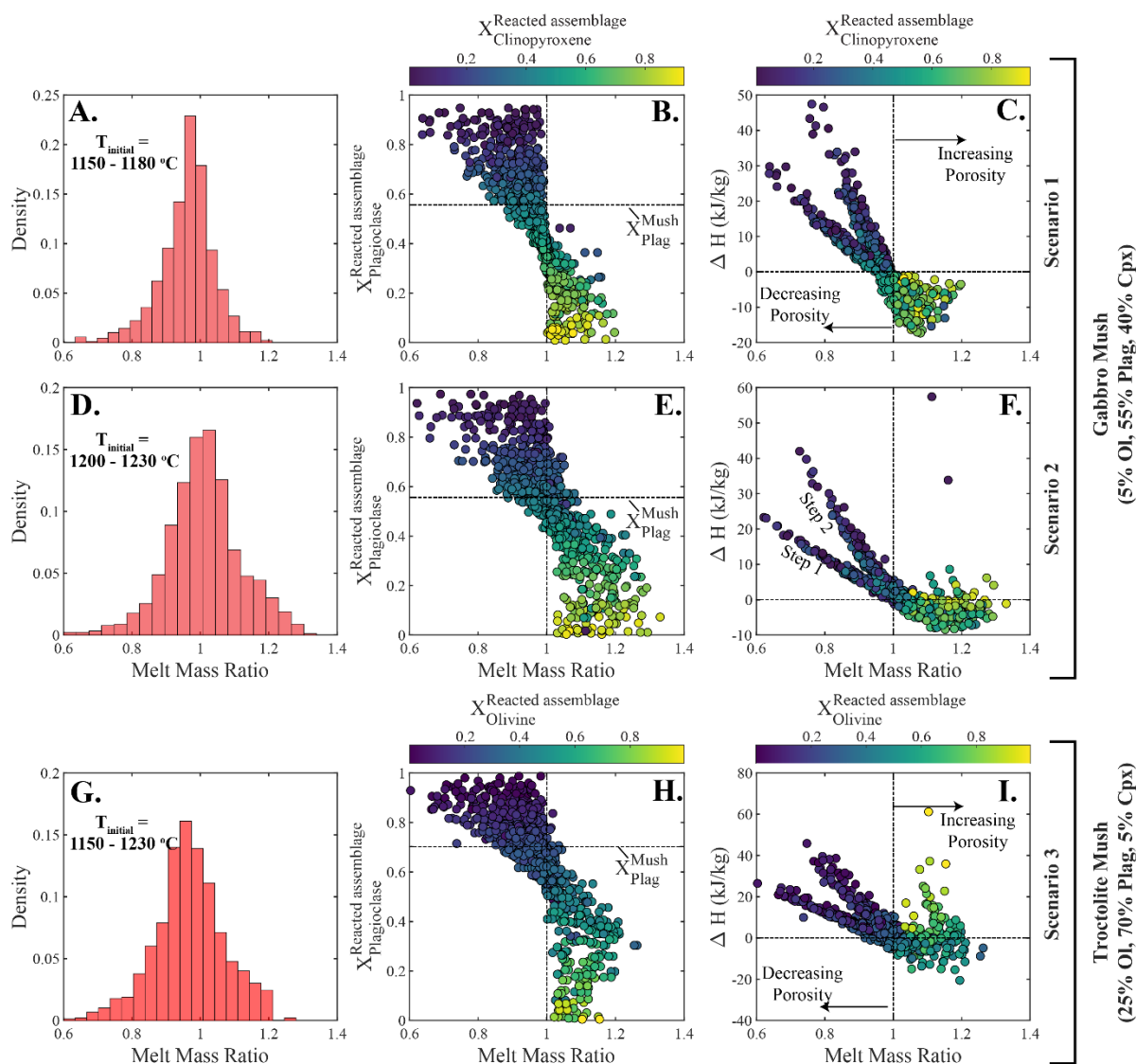


Figure 3 – Reactive flow controls on the system porosity. The change in the melt mass through a reaction is described as $\frac{Mass_{Final}^{melt}}{Mass_{Initial}^{melt}}$ (Melt Mass Ratio), and is compared to the proportion of plagioclase in the reacted solid assemblage ($X_{Plagioclase}^{Reacted\ assemblage}$) and the change in the specific enthalpy of the melt phase (ΔH). Each simulation (450 per scenario) was allowed to run for 2 steps of melt-mush reaction. **A. - C.** Scenario 1: melt-mush reaction simulations involving an ol+plag+cpx saturated basaltic melt. Results indicate that the Melt Mass Ratio during reactions tend to be clustered around 0.95 - 1 (**A.**). There is a strong negative correlation between the Melt Mass Ratio and the proportion of plagioclase in the assimilated assemblage (**B.**), likely associated with the change in the specific enthalpy of the melt phase (**C.**). **D. - F.** Scenario 2: high-temperature models, otherwise equivalent to scenario 1, where the initial melt phase is saturated in olivine and plagioclase. All results (for a given reacted mineralogy) are shifted to slightly higher Melt Mass Ratios than in Scenario 1. **G. - I.** Scenario 3: the mineralogy of the mush system represents a troctolite, rather than a gabbro. The Melt Mass Ratio increases with decreasing proportions of plagioclase in the reacted assemblage. All models were run at 100 MPa.

163 influence the mineralogy of the reacted assemblage contributing to the reactions (as discussed
164 below), but these factors are poorly constrained and thus not incorporated into our models.

165 All scenarios reveal a clear correlation between the Melt Mass Ratio and the proportion of plagioclase
166 in the reacted assemblage ($X_{reaction}^{Plagioclase}$). This correlation is driven by the large latent heat component
167 of plagioclase (relative to olivine and clinopyroxene)⁵⁰, and the change in the specific enthalpy of the
168 melt phase during plagioclase-dominated reactions (Fig. 3). Specifically, when $X_{reaction}^{Plagioclase} > 0.5 -$
169 0.7 , the positive change in the specific enthalpy of the melt phase requires excess crystallisation to
170 balance the enthalpy of the system, and thus drives a decrease in the system porosity. When
171 $X_{reaction}^{Plagioclase} < 0.4 - 0.6$, however, the Melt Mass Ratio is often ~ 1 or > 1 , indicating that the porosity
172 is either constant, maintaining the flux of melt through the system, or increasing, enhancing melt
173 transport (Fig. 3).

174 In addition, offsets between scenario 1 and 2 simulations reveal that the phase saturation of the melt
175 component (i.e., the mineral phases that are stable at the liquidus) also plays an important role in the
176 porosity evolution of a mush. Specifically, our models show that interaction of olivine- and plagioclase-
177 saturated, but clinopyroxene-undersaturated melts with a gabbroic mush system can cause an
178 increase in the system porosity as long as $X_{reaction}^{Plagioclase} < 0.6$ (Scenario 2), whereas this transition
179 occurs at ~ 0.4 for melts saturated in a cotectic phase assemblage of olivine, plagioclase and
180 clinopyroxene (Scenario 1; Fig. 3). The offset between the two scenarios is related to the high latent
181 heat component of plagioclase, which forms a larger proportion of the crystallizing assemblage for
182 models where the initial melt phase is clinopyroxene-undersaturated (Supplementary Information).
183 Consequently, less crystallization (of a plagioclase-rich assemblage) is required to balance the enthalpy
184 of the system. Overall, these results indicate that melt transport through magmatic mush zones can
185 be maintained, or even enhanced by reactive flow in situations where either the melt phase is
186 clinopyroxene-undersaturated or plagioclase does not dominate the dissolved solid assemblage.

187 To investigate this further, we simulate recharge of clinopyroxene-undersaturated melt into a
188 gabbroic mush zone by modifying our model to consider multiple episodes of melt-mush reaction of
189 a single volume of crystal mush. Results confirm that, if there is a sufficient flux of new melt into the
190 mush to maintain clinopyroxene-undersaturation and/or clinopyroxene remains the dominant
191 component in the reacted assemblage, this process will cause a dramatic increase in mush porosity
192 (Fig. 4).

193 However, melt-mush reaction will not always maintain or enhance melt transport: in systems where
194 $X_{reaction}^{Plagioclase} > 0.5 - 0.7$ reactive flow will cause a decrease in the porosity of the system. Critically,

195 experimental analysis of mineral dissolution rates indicates that plagioclase dissolution occurs at a
196 faster rate than that of olivine or clinopyroxene, and that the activation enthalpy of dissolution for
197 plagioclase is typically smaller than that of olivine^{39,40,49}, indicating that this situation may be favoured
198 in many natural systems. Additionally, several petrological studies have shown that key trace element
199 signatures of reactive flow, including the anomalously enriched compositions in clinopyroxene crystal
200 rims^{30,36}, can be reproduced by models where $X_{reaction}^{Plagioclase} > 0.5$. Therefore, we suggest that
201 plagioclase-dominated reactions – that is, excess plagioclase dissolution relative to the modal
202 proportions of plagioclase in the mush – might be the norm in cooling natural systems (outside of the
203 influence of recharging melts etc.). If so, reactive flow of 3-phase saturated magmas within gabbroic
204 mush systems could be partially responsible for the solidification of magmatic mushes, as well as the
205 generation of enriched rims of low-An plagioclase and and low-Mg# clinopyroxene beneath mid-ocean
206 ridges, reducing the requirement of crystal compaction in generating cumulate rocks from cumulate
207 mush.

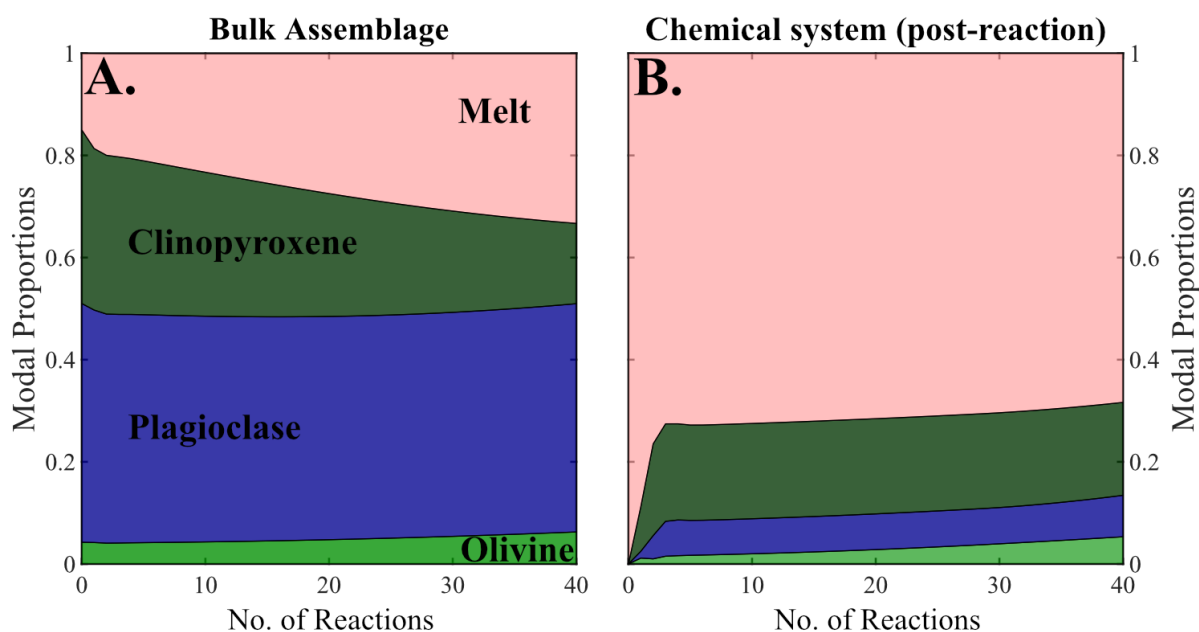


Figure 4 – Results of melt-mush reaction caused by repeated infiltration of clinopyroxene-undersaturated melts. **A.** Phase proportions in the entire mush system (i.e., melt, reacted solids and unreacted solid assemblage). **B.** Phase proportions excluding solid material that remains chemically isolated from the melt phase (i.e., unreacted solid material). In essence, this panel represents the phase proportions of the reaction at each step of the model. Prior to any model reactions (step 0), the local chemical subsystem is composed entirely of melt. The clinopyroxene-undersaturated nature of the melt phase entering the mush system is assumed to drive clinopyroxene dissolution; as a result, clinopyroxene forms the dominant component within the reacted solid component (0.7) and the melt fraction of the mush increases with each reaction. If this process were to continue, it may be expected that the decrease in crystal-fraction of the mush could eventually lead to partial remobilisation or channelisation within the mush system.

208 DISCUSSION

209 IMPLICATIONS FOR MELT TRANSPORT IN NATURAL SYSTEMS

210 Compaction of crystal mush, which has long been postulated to be responsible for the formation of
211 eruptible magma bodies and cumulate rocks^{33,51}, drives porous flow of melts out of the initial mush to
212 accommodate its compaction. Because melts are unlikely to be in equilibrium with the entirety of the
213 solid matrix that they traverse, this porous flow may be reactive. As the Melt Mass Ratio of most
214 reaction is typically centered around 0.95 – 1 (Fig. 3), our findings indicate that porous flow might
215 continue with little-to-no change in porosity and effectively contribute to the formation of melt-rich
216 magma reservoirs and complementary cumulates within crystal-rich systems through compaction.

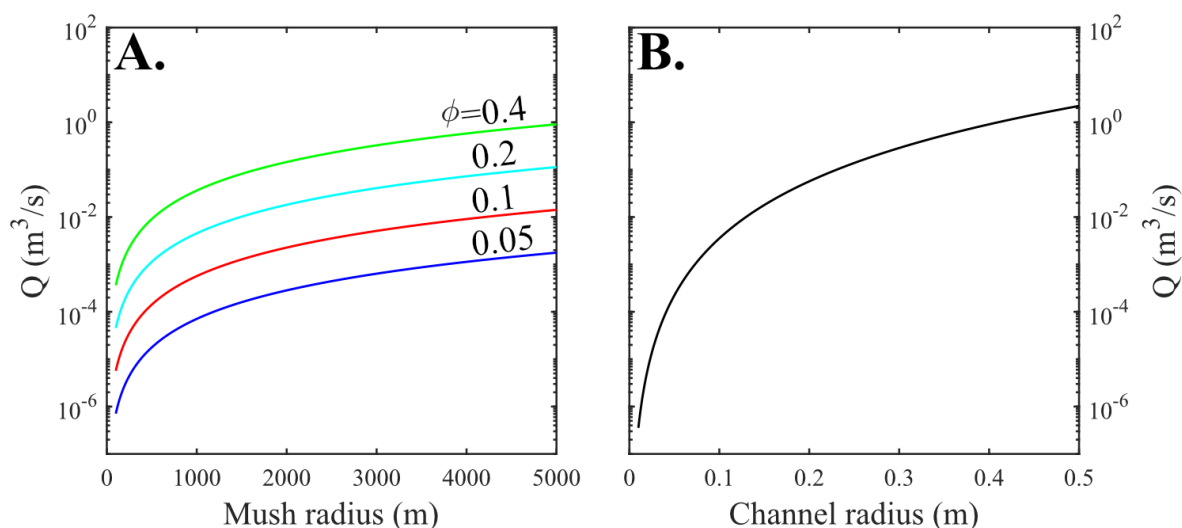


Figure 5 – Volumetric flux of magma through mush systems by either porous flow (A.) or channelized melt flow (B.). These calculations demonstrate that channelized melt flow – with channel radii between 10 and 30 cm – can match the volumetric flux of melt through a crystal mush system 1 – 3km in radius with a porosity between 0.1 and 0.4. Volumetric flux calculations are performed using the equations displayed in the Methods section, with phase densities taken from the alphaMELTS for MATLAB fractional crystallisation model at 1180 °C and the mush density calculated using the modal proportions used in scenarios 1 and 2 (ol₅:plag₅₅:cpx₄₀). The viscosity of the melt phase is calculated in the Python3 tool Thermobar⁵⁷ using the melt viscosity model of Giordano et al.⁵⁸ at 1180 °C and the liquid composition from alphaMELTS for MATLAB.

217 Evidence from natural systems, however, indicates that alternative mechanisms of melt transport are
218 required beyond distributed porous flow. For example, in many fossilized mid-ocean ridge magma
219 reservoirs, erupted lavas and sheeted dykes are in Fe-Mg equilibrium with deep, primitive regions of
220 the mush, but not with the shallower, more evolved sections^{10,52,53}. This observation necessitates rapid
221 and efficient transfer of melt through the magmatic mush to avoid magma re-equilibration with the
222 more evolved, shallower gabbros. As such, melt transport by distributed porous flow cannot explain
223 these compositional relationships, indicating that channelized melt flow is required¹⁰. As dykes are

224 rarely observed crosscutting MOR plutonic sections, this rapid transport must occur at supersolidus
225 conditions, likely in the form of melt channels.

226 Melt channels generated by focused porous flow have been observed on a centimetre- to metre-scale
227 in oceanic core complexes and ophiolites^{37,43}. A reactive origin to these channels is supported by their
228 diffuse channel boundaries, mineral compositions indicative of reaction (e.g., clinopyroxene Ti-Cr
229 relationships³⁰), and the absence of a shape-preferred orientation in the surrounding crystal mush
230 (indicating limited local deformation driving magmatic flow)^{30,37}. Whether such channels also operate
231 on larger scales, like their dunite counterparts in the mantle⁵⁴, remains to be determined.
232 Nonetheless, simple back-of-the-envelope calculations confirm that buoyant melt flow within
233 channels is capable, in principle, of transporting significant amounts of magma through magmatic
234 mush systems. For example, the volumetric flux of a buoyant melt within a single 20 cm radius channel
235 is equivalent to that estimated for distributed porous flow through a cylindrical mush system ~3 km
236 in radius with 20% porosity (~0.05 m³/s; Fig. 5). Our models confirm that reactive flow can drive a
237 dramatic increase in mush porosity and potentially contribute to the formation of these channels.
238 Specifically, increases in mush porosity are likely when clinopyroxene is not on the liquidus and/or
239 olivine or clinopyroxene dissolution occurs at a greater rate than that of plagioclase (Fig. 3). In
240 troctolitic mush systems, olivine dissolution and removal during melt-mush reaction, alongside
241 precipitation of secondary clinopyroxene in channel structures, has been observed⁴³, and could
242 indicate increasing mush porosity and the formation of melt channels during reactive flow. In gabbroic
243 systems, clinopyroxene-undersaturated melts might drive increased dissolution of clinopyroxene,
244 with both factors acting to increase the system porosity. Therefore, we suggest that an increase in
245 gabbro mush porosity, and potentially the formation of melt channels, is likely during reactive flow at
246 high temperatures, prior to clinopyroxene crystallisation (typically >1180 - 1200°C for MORBs).

247 One scenario that promotes interaction of a high-temperature, clinopyroxene-undersaturated magma
248 with a magmatic mush is replenishment; hence, we suggest that rapid, focused melt extraction may
249 be linked to replenishment episodes. Clinopyroxene dissolution following magma replenishment has
250 recently been documented using high resolution chemical mapping and trace element analysis of large
251 clinopyroxene oikocrysts in the Pacific lower oceanic crust⁵⁵. Our models demonstrate that this
252 process (that is, dissolution of a clinopyroxene-bearing assemblage by a high-temperature,
253 clinopyroxene-undersaturated replenishing melt), combined with the advective and conductive
254 transfer of heat energy into the mush from the new replenishing melt, will drive an increase in the
255 system porosity. Natural variations in the initial mush porosity or mineralogy could then lead to spatial
256 heterogeneity in the rate at which the mush porosity increases, focusing of further melt flow and,
257 ultimately, the formation of a reactive melt channel. Alternatively, dramatic increases in the system

258 porosity surrounding a melt lens formed from a replenishing melt could contribute to mush
259 destabilisation and trigger channelized melt transport (Fig. 6).

260 Once a channel is formed, our models indicate that reactive transport can proceed unimpeded if
261 $X_{reaction}^{Plagioclase}$ remains low (<0.4 - 0.6). However, if $X_{reaction}^{Plagioclase}$ increases, the reactions will drive a
262 decrease in the system porosity limiting future melt transport and possibly generating the extreme
263 chemical enrichment observed in mineral rim zones^{30,36,41}.

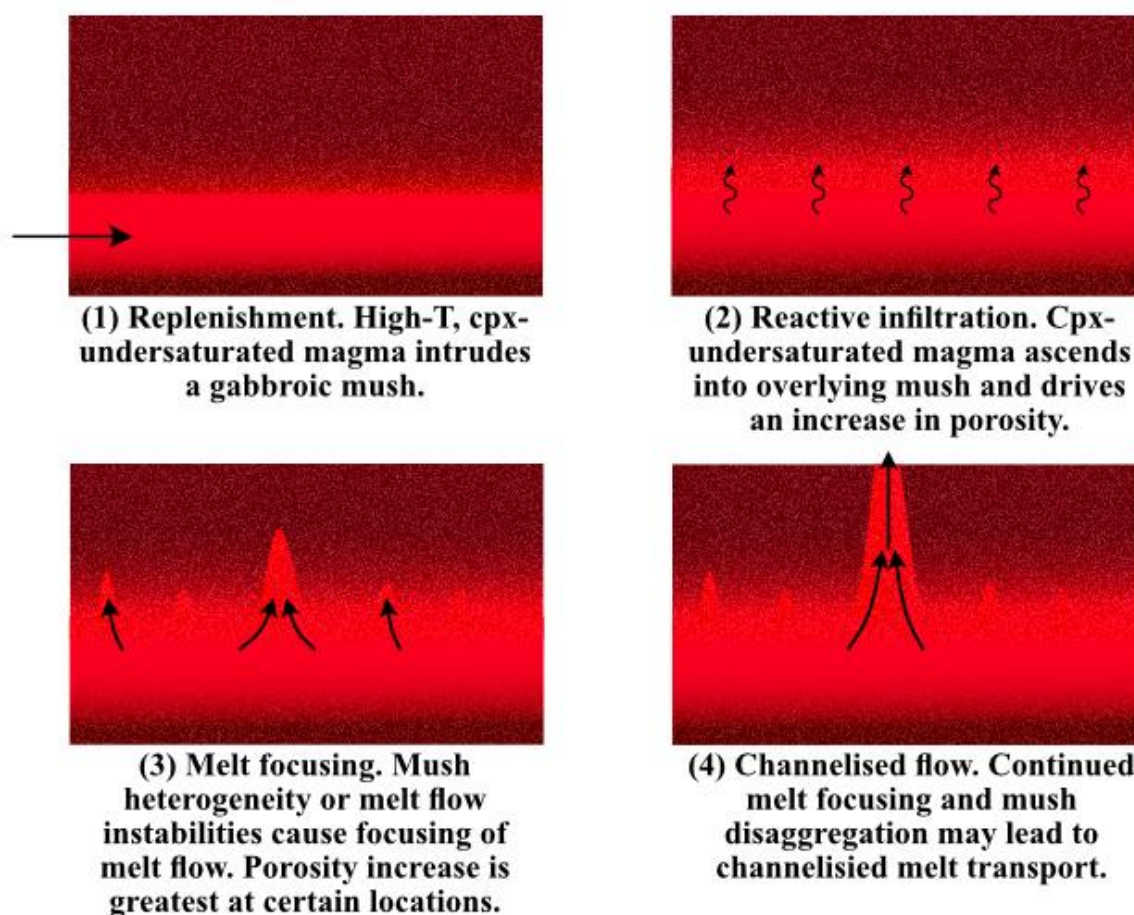


Figure 6 – Schematic representation of the processes leading to melt channelization after magma replenishment (1). The replenishing magma infiltrates into the overlying mush and drives an increase in porosity due to the phase stability of the melt and the presence of clinopyroxene in the reacted solid assemblage (2). Heterogeneity in the mush system, or melt flow instabilities could lead to focusing of melt flow into specific region of the mush (3). Melt focusing could ultimately lead to the generation of a melt channel and rapid transfer of magmas within mush reservoirs (4).

264 BROADER IMPLICATIONS

265 Overall, our results demonstrate that reactive flow can have substantial impacts on the porosity of
266 magmatic mush systems, with implications for the efficiency of melt transport and the viscosity of
267 magmatic reservoirs. This work also highlights that more detailed chemical interactions, which
268 account for variations in the mineralogy of the mush and phase saturation of the melt, must be

269 considered in larger, reservoir-scale models of reactive flow and melt transport to fully capture the
270 dynamics of chemically heterogeneous and complex magmatic systems. At present, large-scale
271 models that account for melt and crystal transport in km-scale magmatic systems contain only very
272 simple chemical parameterisations, with all solid material described by a single composition at
273 temperatures above the solidus^{33,34}. Our results, however, demonstrate that the heterogeneous,
274 multi-component nature of natural mush systems is critical for accurately modelling the influence of
275 reactive flow and evolution of porosity within magmatic mush systems.

276 ACKNOWLEDGEMENTS

277 This work was supported by a Research Fellowship awarded to M.G. by the Royal Commission for the
278 Exhibition of 1851. C.J.L.'s work on reactive flow was supported by NERC grant NE/I001670/1. P.A. was
279 supported by NSF grant EAR-1947616. We are grateful to Valentin Basch and an anonymous reviewer
280 for their helpful and constructive comments on the manuscript.

281 DATA AVAILABILITY

282 All code developed in this study is available via the lead-author's GitHub
283 (<https://github.com/gleesonm1/MeltMushRxn>) and the current version used in this publication has
284 been archived using Zenodo (<https://doi.org/10.5281/zenodo.7626521>). The GitHub repository is set
285 up with a Results folder containing MATLAB script that will recreate the figures shown in this
286 manuscript, allowing readers to investigate the results of our models in detail.

287 REFERENCES

- 288 1. Brown, G. M. The layered ultrabasic rocks of Rhum, Inner Hebrides. *Philos. Trans. R. Soc. Lond. B.*
289 *Biol. Sci.* **240**, 1–53 (1956).
- 290 2. Daly, R. A. The Nature of Volcanic Action. *Proc. Am. Acad. Arts Sci.* **47**, 47 (1911).
- 291 3. Marsh, B. D. Magma Chambers. *Annu. Rev. Earth Planet. Sci.* **17**, 439–472 (1989).
- 292 4. Sparks, R. S. J. *et al.* Formation and dynamics of magma reservoirs. *Philos. Trans. R. Soc. Math.*
293 *Phys. Eng. Sci.* **377**, 20180019 (2019).
- 294 5. Cashman, K. V., Sparks, R. S. J. & Blundy, J. D. Vertically extensive and unstable magmatic systems:
295 A unified view of igneous processes. *Science* **355**, eaag3055 (2017).
- 296 6. Edmonds, M., Cashman, K. V., Holness, M. & Jackson, M. Architecture and dynamics of magma
297 reservoirs. *Philos. Trans. R. Soc. Math. Phys. Eng. Sci.* **377**, 20180298 (2019).

- 298 7. Marsh, B. A magmatic mush column rosetta stone: The McMurdo Dry Valleys of Antarctica. *Eos*
299 *Trans. Am. Geophys. Union* **85**, 497 (2004).
- 300 8. Hildreth, W. & Moorbath, S. Crustal contributions to arc magmatism in the Andes of Central Chile.
301 *Contrib. Mineral. Petrol.* **98**, 455–489 (1988).
- 302 9. Bachmann, O. On the Origin of Crystal-poor Rhyolites: Extracted from Batholithic Crystal Mushes.
303 *J. Petrol.* **45**, 1565–1582 (2004).
- 304 10. Lissenberg, C. J., MacLeod, C. J. & Bennett, E. N. Consequences of a crystal mush-dominated
305 magma plumbing system: a mid-ocean ridge perspective. *Philos. Trans. R. Soc. Math. Phys. Eng.*
306 *Sci.* **377**, 20180014 (2019).
- 307 11. Detrick, R. S. *et al.* Multi-channel seismic imaging of a crustal magma chamber along the East
308 Pacific Rise. *Nature* **326**, 35–41 (1987).
- 309 12. Kent, G. M. *et al.* Evidence from three-dimensional seismic reflectivity images for enhanced melt
310 supply beneath mid-ocean -ridge discontinuities. *Nature* **406**, 614–618 (2000).
- 311 13. Sinton, J. M. & Detrick, R. S. Mid-ocean ridge magma chambers. *J. Geophys. Res.* **97**, 197 (1992).
- 312 14. Langmuir, C. H., Bender, J. F. & Batiza, R. Petrological and tectonic segmentation of the East Pacific
313 Rise, 5°30'–14°30' N. *Nature* **322**, 422–429 (1986).
- 314 15. Sinton, J. M., Smaglik, S. M., Mahoney, J. J. & Macdonald, K. C. Magmatic processes at superfast
315 spreading mid-ocean ridges: Glass compositional variations along the East Pacific Rise 13°–23°S. *J.*
316 *Geophys. Res. Solid Earth* **96**, 6133–6155 (1991).
- 317 16. Kilgour, G., Blundy, J., Cashman, K. & Mader, H. M. Small volume andesite magmas and melt–
318 mush interactions at Ruapehu, New Zealand: evidence from melt inclusions. *Contrib. Mineral.*
319 *Petrol.* **166**, 371–392 (2013).
- 320 17. Wieser, P. E., Edmonds, M., Maclennan, J. & Wheeler, J. Microstructural constraints on magmatic
321 mushes under Kīlauea Volcano, Hawai'i. *Nat. Commun.* **11**, 14 (2020).

- 322 18. Gleeson, M. L. M., Gibson, S. A. & Stock, M. J. Upper mantle mush zones beneath low melt flux
323 ocean island volcanoes: insights from Isla Floreana, Galápagos. *J. Petrol.* ega094 (2020)
324 doi:10.1093/petrology/egaa094.
- 325 19. Stock, M. J. *et al.* Cryptic evolved melts beneath monotonous basaltic shield volcanoes in the
326 Galápagos Archipelago. *Nat Commun* **11**, 3767 (2020).
- 327 20. Passmore, E., Maclennan, J., Fitton, G. & Thordarson, T. Mush Disaggregation in Basaltic Magma
328 Chambers: Evidence from the ad 1783 Laki Eruption. *J. Petrol.* **53**, 2593–2623 (2012).
- 329 21. Neave, D. A., Passmore, E., Maclennan, J., Fitton, G. & Thordarson, T. Crystal–Melt Relationships
330 and the Record of Deep Mixing and Crystallization in the ad 1783 Laki Eruption, Iceland. *J. Petrol.*
331 **54**, 1661–1690 (2013).
- 332 22. Cooper, G. F., Davidson, J. P. & Blundy, J. D. Plutonic xenoliths from Martinique, Lesser Antilles:
333 evidence for open system processes and reactive melt flow in island arc crust. *Contrib. Mineral.*
334 *Petrol.* **171**, 87 (2016).
- 335 23. Farrell, J., Smith, R. B., Husen, S. & Diehl, T. Tomography from 26 years of seismicity revealing that
336 the spatial extent of the Yellowstone crustal magma reservoir extends well beyond the
337 Yellowstone caldera. *Geophys. Res. Lett.* **41**, 3068–3073 (2014).
- 338 24. Lees, J. M. Seismic tomography of magmatic systems. *J. Volcanol. Geotherm. Res.* **167**, 37–56
339 (2007).
- 340 25. Rasht-Behesht, M., Huber, C. & Mancinelli, N. J. Detectability of Melt-Rich Lenses in Magmatic
341 Reservoirs From Teleseismic Waveform Modeling. *J. Geophys. Res. Solid Earth* **125**, (2020).
- 342 26. McKenzie, D. Compaction and Crystallization in Magma Chambers: Towards a Model of the
343 Skaergaard Intrusion. *J. Petrol.* **52**, 905–930 (2011).
- 344 27. McKenzie, D. The Generation and Compaction of Partially Molten Rock. *J. Petrol.* **25**, 713–765
345 (1984).

- 346 28. Schmidt, M. W., Forien, M., Solferino, G. & Bagdassarov, N. Settling and compaction of olivine in
347 basaltic magmas: an experimental study on the time scales of cumulate formation. *Contrib.*
348 *Mineral. Petrol.* **164**, 959–976 (2012).
- 349 29. Sparks, R. S. J., Huppert, H. E., Kerr, R. C., McKenzie, D. P. & Tait, S. R. Postcumulus processes in
350 layered intrusions. *Geol. Mag.* **122**, 555–568 (1985).
- 351 30. Lissenberg, C. J. & MacLeod, C. J. A Reactive Porous Flow Control on Mid-ocean Ridge Magmatic
352 Evolution. *J. Petrol.* **57**, 2195–2220 (2016).
- 353 31. Holness, M. B. Melt segregation from silicic crystal mushes: a critical appraisal of possible
354 mechanisms and their microstructural record. *Contrib. Mineral. Petrol.* **173**, 48 (2018).
- 355 32. Holness, M. B., Vukmanovic, Z. & Mariani, E. Assessing the Role of Compaction in the Formation
356 of Adcumulates: a Microstructural Perspective. *J. Petrol.* **58**, 643–673 (2017).
- 357 33. Jackson, M. D., Blundy, J. & Sparks, R. S. J. Chemical differentiation, cold storage and
358 remobilization of magma in the Earth's crust. *Nature* **564**, 405–409 (2018).
- 359 34. Solano, J. M. S., Jackson, M. D., Sparks, R. S. J. & Blundy, J. Evolution of major and trace element
360 composition during melt migration through crystalline mush: Implications for chemical
361 differentiation in the crust. *Am. J. Sci.* **314**, 895–939 (2014).
- 362 35. Lissenberg, C. J., MacLeod, C. J., Howard, K. A. & Godard, M. Pervasive reactive melt migration
363 through fast-spreading lower oceanic crust (Hess Deep, equatorial Pacific Ocean). *Earth Planet.*
364 *Sci. Lett.* **361**, 436–447 (2013).
- 365 36. Boulanger, M. *et al.* Magma Reservoir Formation and Evolution at a Slow-Spreading Center
366 (Atlantis Bank, Southwest Indian Ridge). *Front Earth Sci* **8**, 554598 (2020).
- 367 37. Sanfilippo, A., MacLeod, C. J., Tribuzio, R., Lissenberg, C. J. & Zanetti, A. Early-Stage Melt-Rock
368 Reaction in a Cooling Crystal Mush Beneath a Slow-Spreading Mid-Ocean Ridge (IODP Hole
369 U1473A, Atlantis Bank, Southwest Indian Ridge). *Front. Earth Sci.* **8**, 579138 (2020).
- 370 38. Antoshechkina, P. M. & Ghiorso, M. S. MELTS for MATLAB: A new Educational and Research Tool
371 for Computational Thermodynamics. *AGU Fall Meet.* (2018).

- 372 39. Chen, Y. & Zhang, Y. Clinopyroxene dissolution in basaltic melt. *Geochim. Cosmochim. Acta* **73**,
373 5730–5747 (2009).
- 374 40. Chen, Y. & Zhang, Y. Olivine dissolution in basaltic melt. *Geochim. Cosmochim. Acta* **72**, 4756–
375 4777 (2008).
- 376 41. Gao, Y., Hoefs, J., Hellebrand, E., von der Handt, A. & Snow, J. E. Trace element zoning in pyroxenes
377 from ODP Hole 735B gabbros: diffusive exchange or synkinematic crystal fractionation? *Contrib*
378 *Miner. Pet.* **153**, 429–442 (2007).
- 379 42. Coogan, L. A., Saunders, A. D., Kempton, P. D. & Norry, M. J. Evidence from oceanic gabbros for
380 porous melt migration within a crystal mush beneath the Mid-Atlantic Ridge: EVIDENCE FROM
381 OCEANIC GABBROS. *Geochem Geophys Geosyst* **1**, n/a-n/a (2000).
- 382 43. Lissenberg, C. J. & Dick, H. J. B. Melt–rock reaction in the lower oceanic crust and its implications
383 for the genesis of mid-ocean ridge basalt. *Earth Planet. Sci. Lett.* **271**, 311–325 (2008).
- 384 44. Gualda, G. A. R., Ghiorso, M. S., Lemons, R. V. & Carley, T. L. Rhyolite-MELTS: a Modified
385 Calibration of MELTS Optimized for Silica-rich, Fluid-bearing Magmatic Systems. *J. Petrol.* **53**, 875–
386 890 (2012).
- 387 45. Ghiorso, M. S. & Gualda, G. A. R. An H₂O–CO₂ mixed fluid saturation model compatible with
388 rhyolite-MELTS. *Contrib Miner. Pet.* **169**, 53 (2015).
- 389 46. Yang, A. Y., Wang, C., Liang, Y. & Lissenberg, C. J. Reaction Between Mid-Ocean Ridge Basalt and
390 Lower Oceanic Crust: An Experimental Study. *Geochem Geophys Geosyst* **20**, 4390–4407 (2019).
- 391 47. Pfann, W. G. Principles of Zone-Melting. *JOM* **4**, 747–753 (1952).
- 392 48. Harris, P. G. Zone refining and the origin of potassic basalts. *Geochim. Cosmochim. Acta* **12**, 195–
393 208 (1957).
- 394 49. Donaldson, C. H. The rates of dissolution of olivine, plagioclase, and quartz in a basalt melt.
395 *Mineral. Mag.* **49**, 683–693 (1985).
- 396 50. Ghiorso, M. S. THERMODYNAMIC MODELS OF IGNEOUS PROCESSES. *Annu. Rev. Earth Planet. Sci.*
397 **25**, 221–241 (1997).

- 398 51. Lee, C.-T. A., Morton, D. M., Farner, M. J. & Moitra, P. Field and model constraints on silicic melt
399 segregation by compaction/hindered settling: The role of water and its effect on latent heat
400 release. *Am. Mineral.* **100**, 1762–1777 (2015).
- 401 52. Kelemen, P. B., Koga, K. & Shimizu, N. Geochemistry of gabbro sills in the crust-mantle transition
402 zone of the Oman ophiolite: implications for the origin of the oceanic lower crust. *Earth Planet.*
403 *Sci. Lett.* **146**, 475–488 (1997).
- 404 53. Lissenberg, C. J., Loocke, M. P. & Macleod, C. J. The paradox of the axial melt lens: petrology and
405 geochemistry of the upper plutonics at Hess Deep. *AGU Fall Meet.* (2014).
- 406 54. Kelemen, P. B., Shimizu, N. & Salters, V. J. M. Extraction of mid-ocean-ridge basalt from the
407 upwelling mantle by focused flow of melt in dunite channels. *Nature* **375**, 747–753 (1995).
- 408 55. Leuthold, J. *et al.* Partial Melting of Lower Oceanic Crust Gabbro: Constraints From Poikilitic
409 Clinopyroxene Primocrysts. *Front. Earth Sci.* **6**, 15 (2018).
- 410 56. Grove, T. L., Kinzler, R. J. & Bryan, W. B. Fractionation of Mid-Ocean Ridge Basalt (MORB). in
411 *Geophysical Monograph Series* (eds. Morgan, J. P., Blackman, D. K. & Sinton, J. M.) 281–310
412 (American Geophysical Union, 1992). doi:10.1029/GM071p0281.
- 413 57. Wieser, P. *et al.* Thermobar: An open-source Python3 tool for thermobarometry and hygrometry.
414 *Volcanica* **5**, 349–384 (2022).
- 415 58. Giordano, D., Russell, J. K. & Dingwell, D. B. Viscosity of magmatic liquids: A model. *Earth Planet.*
416 *Sci. Lett.* **271**, 123–134 (2008).
- 417 59. Hartlieb, P., Toifl, M., Kuchar, F., Meisels, R. & Antretter, T. Thermo-physical properties of selected
418 hard rocks and their relation to microwave-assisted comminution. *Miner. Eng.* **91**, 34–41 (2016).
- 419 60. Gale, A., Dalton, C. A., Langmuir, C. H., Su, Y. & Schilling, J.-G. The mean composition of ocean
420 ridge basalts: MEAN MORB. *Geochem. Geophys. Geosystems* **14**, 489–518 (2013).
- 421 61. Shorttle, O., MacLennan, J. & Lambart, S. Quantifying lithological variability in the mantle. *Earth*
422 *Planet. Sci. Lett.* **395**, 24–40 (2014).
- 423 62. Turcotte, F. L. & Schubert, G. *Geodynamics*. (Cambridge University Press, 2002).

This preprint is not an accepted peer-reviewed manuscript. A version of this preprint has been resubmitted to *Nature Communications* following one round of peer-review.

424 63. Whitaker, S. Flow in porous media I: A theoretical derivation of Darcy's law. *Transp. Porous Media*
425 1, 3–25 (1986).

426

427 METHODS

428 A THERMODYNAMIC SOLUTION TO MELT-MUSH REACTION

429 We simulate the interaction of basaltic melts with mafic mush systems using the alphaMELTS for
430 MATLAB package and the rhyolite-MELTS v1.0.2 thermodynamic model⁴⁴. Our intention here is not to
431 provide a complete physio-chemical model of melt and crystal transport in magmatic systems, but to
432 construct a thermodynamic framework with which to evaluate the physical consequences of reactive
433 flow.

434 We use our new code to develop two models of melt-mush reaction. The first considers the evolving
435 nature of a melt phase as it passes through a magmatic system and chemically interacts with multiple
436 regions of mush (Figs. 1 & 3); i.e., the melt composition formed in each reaction proceeds into a new
437 region of uninfluenced mush where melt-mush reaction occurs again. The second model focuses on a
438 single mush horizon and considers the influence of several episodes of melt-mush reaction (due to
439 ongoing melt flow into the mush) on the mineralogy, composition, and porosity of that region (Fig. 4).

440 To ensure the results of these models are appropriate to natural system, we must consider both the
441 local chemical system within which the reaction occurs (melt + solid reactants) as well as the thermal
442 properties of the wider mush system. This is because, chemical mapping of natural cumulate samples
443 reveals the presence of 'relict' crystal cores that appear to be uninfluenced by melt-mush reaction,
444 indicating that complete chemical equilibrium across the mush system is rarely achieved^{30,37}. As a
445 result, we define 2 chemical sub-systems, one characterized by a melt phase and the solid material
446 involved in the reaction (i.e., the dissolved assemblage), and the second characterized by an unreacted
447 solid assemblage. However, as the thermal diffusivity of basaltic melts and mafic mineral phases is
448 several orders of magnitude greater than the chemical diffusivities that control mineral dissolution
449 rates^{39,49,59}, we assume that the local mush system (including both the unreacted solid assemblage
450 and the active chemical system) remains in thermal equilibrium during melt-mush reaction. Therefore,
451 to determine the new equilibrium assemblage for the mush system following melt-mush reaction we
452 consider both the chemistry of the local subsystems and the energy balance across the mush (i.e., the
453 unreacted solid assemblage may act to buffer any temperature variations caused by melt-mush
454 reaction).

455 Our new models of reactive flow and melt-mush reaction require several key independent variables
456 to be specified by the user, such as the temperature and pressure of the mush system prior to reactive
457 flow ($T_{initial}$, P). Our model also offers the opportunity to provide a temperature offset between the
458 mush and the percolating melt phase (ΔT), but this is set at 0 for all calculations shown in this study.

459 Other variables include the initial melt mass fraction of the mush system (φ ; taken here to broadly
460 represent the mush porosity) and the mass of solid material involved in the reaction relative to the
461 mass of melt in the system (M ; i.e., the mass of dissolved solid material), which can also be used to
462 describe the melt/solid ratio of the reaction ($1/M$). These two variables are critical as they can be used
463 to define the relative mass of the three key components within the system: solid material within the
464 mush that remains isolated from reaction ($1 - \varphi * (1 + M)$), the mass of solid material that reacts
465 with the percolating melt ($\varphi * M$), and the mass of melt (φ).

466 The composition of the initial melt phase and the solid phases in the mush system must also be
467 specified (C_{phase}). In addition, it is also necessary to define the mineralogical proportions in the mush
468 (X_{phase}^{Mush}) and the relative mineral proportions in the reacted assemblage (X_{phase}^{React}). Notably, we define
469 these two variables separately, which allows us to investigate the influence of additional factors such
470 as variations in dissolution rates (leading to excess incorporation of a single phase into the reaction).
471 Once these variables have been defined, we can use the rhyolite-MELTS v1.0.2 thermodynamic model,
472 implemented through alphaMELTS for MATLAB, to simulate reactive flow^{44,45}.

473 To simulate reactive flow, we first perform a simple fractional crystallisation calculation to convert the
474 melt composition provided by the user into a related magmatic composition at the model specified
475 temperature. These fractional crystallisation models initiate at the liquidus of the user-provided melt
476 phase and terminate at the temperature specified for the reactive flow models. At this point, the
477 composition and specific enthalpy of the melt phase, critical for the following calculations, are
478 extracted from the fractional crystallisation models.

479 Next, we use the specified values of M , φ , X_{phase}^{Mush} , X_{phase}^{React} , and the composition of each phase to
480 create 2 chemical systems: the unreacted solid assemblage and the local chemical system of the
481 reaction. In addition, once these chemical subsystems have been defined, we can use the
482 '*calcPhaseProperties*' command in alphaMELTS for MATLAB to calculate the specific enthalpy for each
483 phase in the solid mush; where appropriate, these calculations are performed separately for the solid
484 material that is involved in the chemical reactions and the unreacted solid assemblage. Now that the
485 specific enthalpy of each phase (and each component) within the mush system is known, the total
486 enthalpy of the mush system can be calculated by:

$$487 \quad H^{Mush} = H^{liq} * \varphi + H^{Solid_{unreacted}} * (1 - \varphi * (1 + M)) + H^{Solid_{reacted}} * M * \varphi$$

488 Where H represents the specific enthalpy of each component (J/kg). Within our models, we assume
489 that there is no flux of heat energy into or out of the system during melt-mush reaction and, as these
490 calculations are performed at a constant pressure, this indicates that the value of H^{Mush} must remain

491 constant during the reaction (where $H^{Mush} = H^{Reaction} * \varphi * (1 + M) + H^{Solid_{unreacted}} * (1 - \varphi * (1 + M))$). Therefore, any change in the enthalpy of the local chemical system of the reaction
492 ($H^{Reaction}$) must be balanced by changes in the enthalpy (and therefore temperature) of the
493 unreacted solid assemblage ($H^{Solid_{unreacted}}$) and this constraint is critical for determining the new
494 equilibrium assemblage within the mush.
495

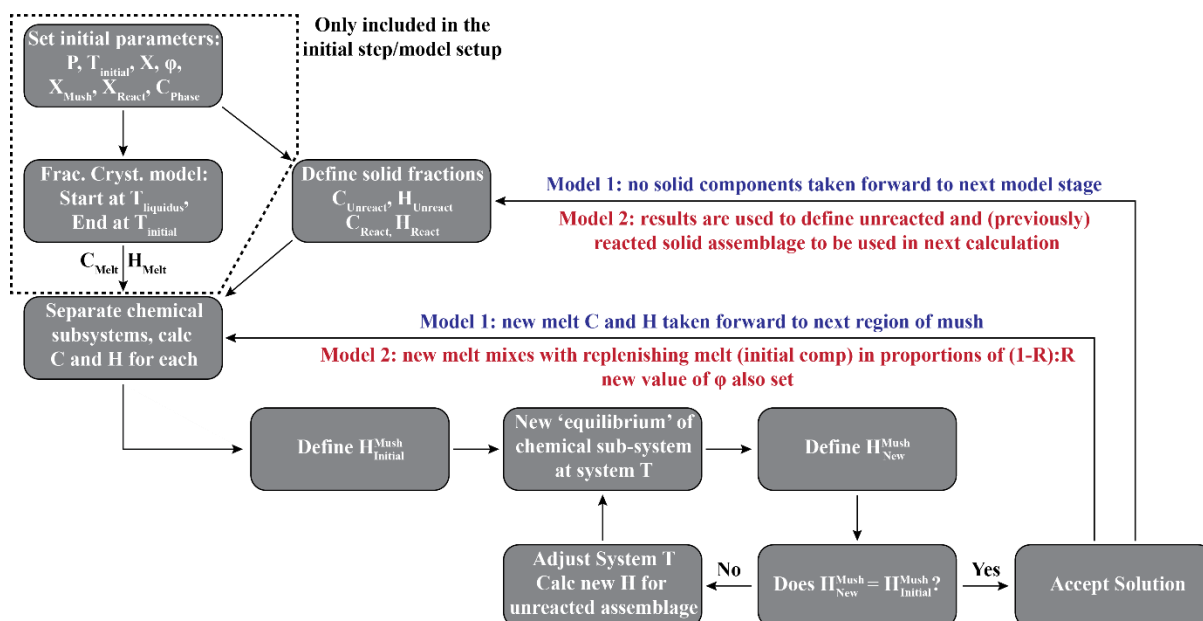
496 In addition to the enthalpy of the mush system, we also need to consider the chemical composition of
497 the local chemical system of the reaction. This is defined as a mixture of the melt phase and the
498 reacted solid assemblage:

$$499 \quad C^{Reaction} = C^{liq} * \frac{\varphi}{\varphi * (1 + M)} + C^{Solid_{reacted}} * \frac{M * \varphi}{\varphi * (1 + M)}$$

500 Once the chemical composition of the reaction is defined, we can proceed to calculate the
501 mineralogical assemblage and phase compositions in the local chemical system following melt-mush
502 reaction. This is achieved using an iterative approach to ensure conservation of energy throughout
503 the reaction (i.e., constant H^{Mush}). First, an initial 'guess' for the post-reaction assemblage is
504 determined at the current temperature of the system and the enthalpy of this new assemblage is
505 recorded ($H_{New}^{Reaction}$). As $H_{New}^{Reaction}$ is unlikely to match the enthalpy of the melt phase and reacted
506 solid assemblage prior to the calculation ($H_{Initial}^{Reaction}$), this initial guess for the post-reaction
507 assemblage will break the constraint that the internal energy of the system (H^{Mush}) must remain
508 constant during the reaction. As a result, we iteratively adjust the temperature of the mush system,
509 and recalculate the post-reaction local equilibrium (and $H_{New}^{Reaction}$) as well as the enthalpy of the
510 unreacted solid assemblage ($H_{New}^{Solid_{unreacted}}$) at each temperature. This process is repeated until
511 $H_{Initial}^{Mush} = H_{New}^{Mush}$, at which point the temperature of the system, alongside the new melt and mineral
512 compositions – as well as their abundances – are recorded. At this point, the process may be repeated,
513 either by taking the new melt composition forward to undergo reaction with a new region of magmatic
514 mush (Model 1; Fig. 1) or by separating the solid fraction of the mush into a reacted and unreacted
515 component, allowing new melt to enter the same region of mush (where the relative fraction of new
516 melt entering the system is defined by a parameter R) and a new reaction to proceed (Model 2; Fig.
517 4).

518 In theory, the model provided in this study is extremely flexible and can easily be expanded to consider
519 other scenarios (e.g., the influence of reactive flow in silicic systems). Simplified MATLAB codes
520 designed to simulate the interaction of basaltic melts with gabbroic mush zones are provided in a
521 GitHub repository and the current version of these models are archived on Zenodo. These models can
522 be easily modified to incorporate different mineral phases, melt compositions, or internal conditions

523 (e.g., temperature and pressure). For the purposes of this study, however, our models are used to
 524 focus on the influence of reactive flow in mid-ocean ridge settings. As a result, in all models provided
 525 here, we use natural data from the South-West Indian Ridge and the nearby Atlantis Bank oceanic
 526 core complex to constrain the composition of the melt and mineral phases in our reactive flow models.
 527 Specifically, we use the mean composition of samples KNO0162-9-048-021GL, KNO0162-9-048-004GL
 528 and AII0107-6-056-028GL (3 of the most primitive basalt compositions from the SWIR) from ~52 – 55
 529 °S on the SWIR as the initial melt composition in our fractional crystallisation and reactive flow models
 530 (compositions taken from the compiled database of Gale et al.⁶⁰). Similarly, the composition of the
 531 mineral phases used in the reactive flow models are taken from the work of Boulanger et al.³⁶ on the
 532 Atlantis Bank oceanic core complex; in detail, we use the average core composition of minerals
 533 measured in olivine-gabbros and troctolites at depths greater than 500 m. Notably, fractional
 534 crystallisation models initiated at our proposed starting composition are able to recreate the major
 535 compositional trends observed in the SWIR basalts, with reactive flow potentially acting to explain
 536 some of the compositional spread around this primary differentiation path (see Supplementary
 537 Information).



Methods Figure – Flow diagram outlining the 2 models developed in this study.

538 Within the simulations shown in Figs. 1 & 3, we used a Bayesian approach to assess the influence of
 539 each parameter on the chemical and physical consequences of reactive porous flow. For all scenarios,
 540 the initial values of $T_{initial}$, M , and ϕ in each simulation were selected from uniform distributions
 541 ($0.05 < M < 0.35$; $0.1 < \phi < 0.35$; T range specified separately for each scenario). The mineralogy
 542 of the mush is set to a constant value within each scenario, but the mineralogy of the dissolved solid
 543 assemblage is allowed to vary. This is done by creating a random value for each mineral phase ranging
 544 from 0 to their modal proportion in the wider mush system and then normalizing the outputted values.

545 For example, in Scenario 1, the code generates random values for olivine, plagioclase, and
546 clinopyroxene between 0 and 0.05, 0.55, and 0.40, respectively. In a single simulation, the code may
547 return hypothetical values of 0.0125, 0.4236, and 0.0890, which when normalised equates to modal
548 proportions in the dissolved solid assemblage of 0.0238, 0.8067, and 0.1695 for olivine, plagioclase,
549 and clinopyroxene, respectively. Which minerals are dissolved by percolating melts in natural systems,
550 and their relative proportions, will likely be influenced by several factors, including the temperature
551 of the system, the relative geochemical enrichment of the percolating melt relative to that which
552 formed in the initial mush (especially as magmas of the lower crust likely retain much of the underlying
553 mantle heterogeneity), and the kinetic barriers to dissolution/reprecipitation. As these factors are
554 difficult to incorporate into our thermodynamic-based models, we believe our Bayesian approach,
555 sampling a wide distribution space, is the most effective means of determining the influence of melt-
556 mush reaction on mush porosity evolution in this study.

557 VOLUMETRIC FLUX CALCULATIONS

558 We provide calculations for the volumetric flux of magma through a mush zone in two different flow
559 regimes. First, we estimate the volumetric flux of magma that can be achieved by buoyancy-driven
560 flow through a high-porosity melt channel. Second, we consider the volumetric flux of magma that
561 results from buoyancy- and compaction-driven flow out of a cumulate mush zone. Comparing the two
562 values provides insights into the role that melt channelization and mush permeability play in the
563 extraction of magma from magmatic mush zones and/or the transfer of magmas within a mush.

564 The volumetric flux of buoyant magma through a high porosity melt channel within a deformable
565 mush zone can be calculated via^{61,62}:

$$566 \quad Q_C = \frac{\pi}{8} \times \frac{\Delta\rho g r^4}{\mu_l}$$

567 Where Q_C is the volumetric flux of magma through the channel (m^3/s); $\Delta\rho$ is the density difference
568 between the mush and the ascending melt phase ($\rho_{melt} - \rho_{mush}$; kg/m^3); g represents gravitational
569 acceleration ($-9.81 m/s^2$); r is the radius of the channel (m); and μ_l is the viscosity of the melt phase
570 ($Pa s$). This equation, relating $\Delta\rho$ and r to the volumetric magma flux, is taken from a simplification
571 of plume flow⁶², but provides meaningful insights into the volumetric flux of magma that can be
572 achieved in a melt channel if the viscosity of the melt is substantially lower than the medium it is
573 passing through. As the mush has a viscosity several orders of magnitude greater than the melt phase,
574 this condition is met. The calculations are performed using a range of different channel radii, other

This preprint is not an accepted peer-reviewed manuscript. A version of this preprint has been resubmitted to *Nature Communications* following one round of peer-review.

575 parameters are taken from alphaMELTS for MATLAB (that is, the density of the different phases) with
576 the exception of the melt viscosity^{57,58} (Fig. 5).

577 In contrast, the volumetric flux of magma through a permeable mush reservoir can be calculated via
578 Darcy's Law⁶³:

$$579 \quad Q_D = \frac{kA}{\mu_l} \times \frac{\Delta P}{\Delta z}$$

580 Where k represents the permeability of the mush zone (m^2); A is the surface area of the mush zone
581 (m^2); and ΔP is the pressure gradient within the mush over vertical height Δz (Pa/m). The pressure
582 gradient generated by density differences between the melt phase and crystal framework within a
583 mush zone can be written as:

$$584 \quad \Delta z = \frac{\Delta P}{\Delta \rho g}$$

585 Therefore, by rearranging the above equations, the volumetric flux of magma through a permeable
586 mush zone can be written as:

$$587 \quad Q_D = \frac{kA}{\mu_l} \times \Delta \rho g$$

588 Where the permeability of the mush zone is calculated using the method outlined by ref.³⁴:

$$589 \quad k = a^2 b \emptyset^\alpha$$

590 Here a represents the typical radius of the grains within the mush zone (m); b is a permeability
591 constant (set to 0.002); α represents a permeability exponent (set to 3); and \emptyset represents the porosity
592 of the mush.

Supplementary Information: Porosity evolution of mafic crystal mush during reactive flow

February 18, 2023

Matthew L. M. Gleeson^{1,2*}, C. Johan Lissenberg¹, Paula Antoshechkina³

¹School of Earth and Environmental Sciences, Cardiff University, Main Building, Park Place, CF10 3AT, UK.

²Department of Earth and Planetary Science, University of California Berkeley, McCone Hall, Berkeley, CA 94720, USA

³Division of Geological and Planetary Sciences, Caltech, Pasadena, CA, 91125, USA

*Corresponding author: gleesonm@berkeley.edu

Controls on porosity changes

In the main text, we demonstrate that changes in mush porosity during reactive flow are dominantly controlled by the mineralogy of the dissolved solid assemblage. By considering other variables in the melt-mush reaction models we can also examine why these changes are so critical. Correlation matrices for each scenario modelled (shown in the main text and repeated below) confirm that there is a strong correlation between the Melt Mass Ratio and the proportion of plagioclase and clinopyroxene (or olivine for a troctolitic mush) in the dissolved solid assemblage (Fig. 1). However, these calculations also show that the Melt Mass Ratio is correlated with the mineralogy of the crystallised assemblage (unsurprisingly as this is strongly linked to the mineralogy of the dissolved assemblage) and the change in specific enthalpy of the melt phase (ΔH).

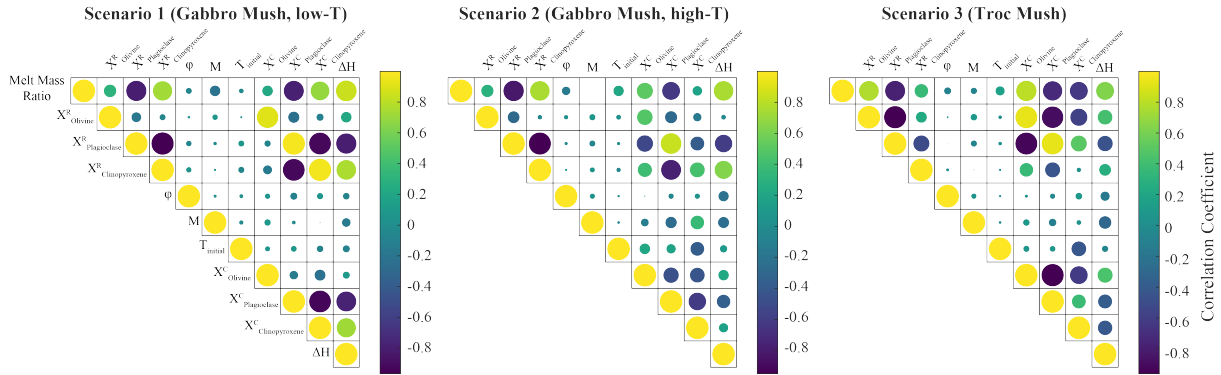


Figure 1: Correlation matrices for each scenario. In all models, there is a strong correlation between the Melt Mass Ratio, the proportion of plagioclase in the dissolved solid assemblage ($X^R_{Plagioclase}$), and the change of specific enthalpy in the melt phase (ΔH defined as the difference between the specific enthalpy of the melt phase prior to, and after melt-mush reaction). There are, however, subtle differences between the scenarios. For example, in scenario 2, there is a weaker correlation between the proportion of clinopyroxene in the crystallised assemblage ($X^C_{Clinopyroxene}$) and the Melt Mass Ratio than there is in scenario 1. This is likely due to the higher temperature of the scenario 2 models and the clinopyroxene-undersaturated nature of the initial melt phase (and thus lower contribution of clinopyroxene to the crystallising assemblage).

In our models, we require that the enthalpy of the entire mush system remains constant (to simulate a thermally equilibrated mush system). As a result, subtle changes in the enthalpy of the melt phase can have significant impacts on the porosity of the mush system. To examine this in more detail, we provide three model runs with plagioclase:clinopyroxene:olivine proportions in the reacted solid assemblage of 75:20:5, 55:40:5, and 25:70:5 (a gabbroic mineralogy is assumed for the wider mush system). Our results indicate that in models dominated by plagioclase dissolution, the difference in enthalpy between the melt phase and dissolved and crystallised solid assemblages increases during melt-mush reaction (Fig. 2). As a result, to maintain the total enthalpy of the mush system, excess crystallisation is required and thus a decrease in the mush porosity. In contrast, when clinopyroxene is dominant, the enthalpy of the melt phase tends towards the enthalpy of the dissolved and crystallised solid assemblages,

meaning that less crystallisation is required to balance the enthalpy of the mush system (and thus an increase in mush porosity).

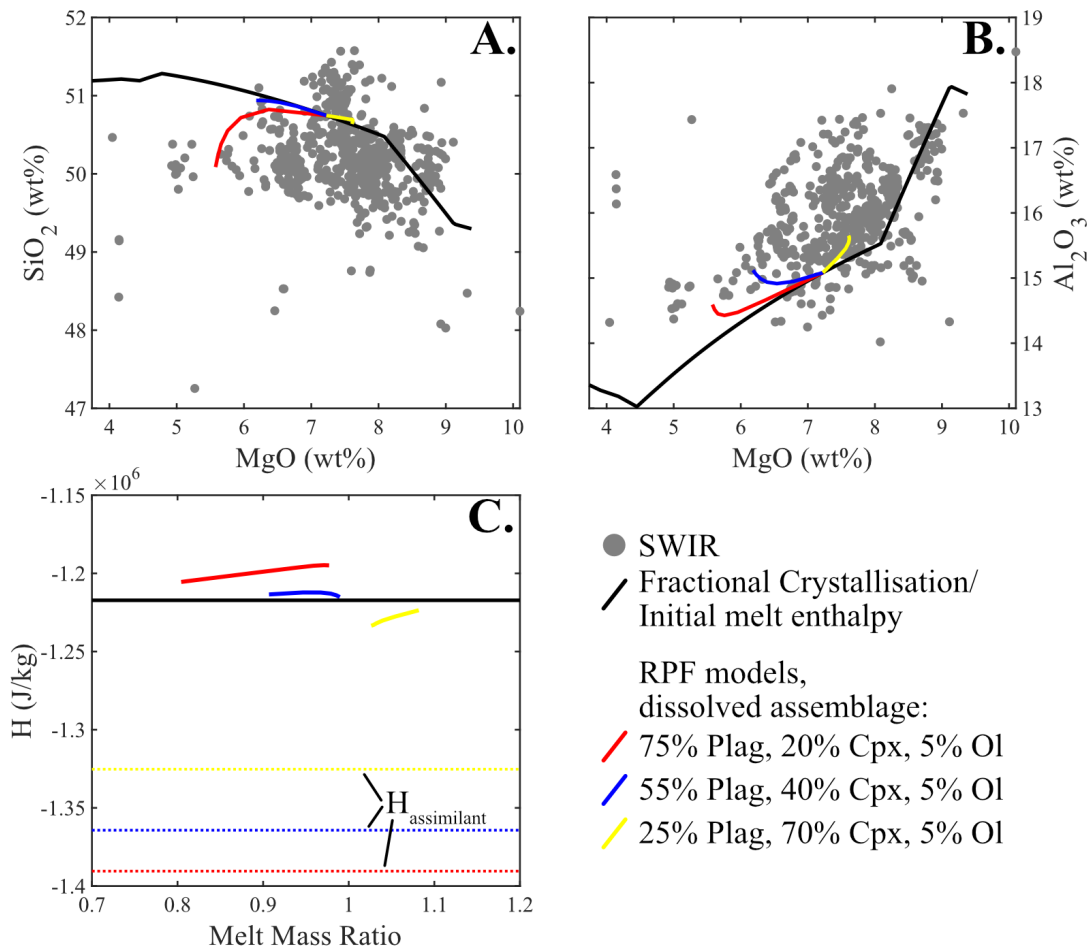


Figure 2: Data shown in **A.** and **B.** represent mid-ocean ridge basalt data of the South-West Indian Ridge from the compilation of Gale et al. (2013). The fractional crystallisation model shown is the same as that used in Fig. 3 of the main text. The reactive flow models initiate at a temperature of 1180 °C, with an initial mush porosity of 0.2 and $M = 0.3$. **A.** and **B.** demonstrate that the melt composition during reactive flow deviates from the path defined by fractional crystallisation. **C.** the difference between the enthalpy of the melt phase and the dissolved solid assemblage increases during melt-mush reaction in models where plagioclase forms a dominant component of the dissolved solid assemblage (>50%). This drives excess crystallisation and a decrease in mush porosity.

Mineralogical changes in the mush

One of the key predictions regarding melt-mush reaction in the literature is that it causes a net change in the mineralogy of the affected mush systems. In fact, several studies have proposed that reactive porous flow in gabbroic mush systems might be characterised by a net increase in the modal proportion of clinopyroxene within the mush system (e.g., equation 1 in Lissenberg et al. 2016).

Using our new models we can evaluate the change in the mineralogy of the mush system as a result of reactive flow and melt-mush reaction. Our results indicate that for the base scenario (i.e., porous flow of a three-phase saturated magma through a gabbroic mush system: Scenario 1), we see a net increase in the proportion of clinopyroxene in the mush system at the expense of plagioclase (Fig. 3). In Scenario 2, where the initial melt phase is clinopyroxene undersaturated, a net increase in the modal proportion of plagioclase in the mush is typically observed, potentially aiding the increase in the porosity of the system found in many of these models due to the high latent heat component of plagioclase (Fig. 3). In addition, our results demonstrate that in Scenarios 1 & 3 there is a net increase in the proportion of mafic minerals (olivine + clinopyroxene) relative to plagioclase in the mush. As a result, when the proportion of plagioclase in the reacted assemblage is low (<0.2), little or no plagioclase is expected in the crystallising assemblage, explaining the peak at 0 in panel **H.** of the histograms below.

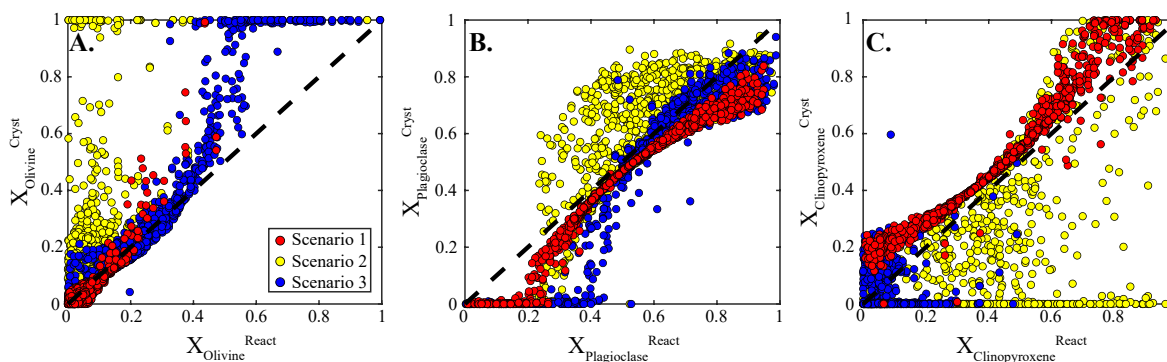


Figure 3: Changes in the mineralogy of the mush, expressed as the proportion of olivine (**A.**), plagioclase (**B.**), and clinopyroxene (**C.**) in the reacted (x-axis) and crystallised (y-axis) assemblage. When data falls above the 1:1 line, this indicates an increase in the proportion of that mineral in the final mush system. For Scenarios 1 & 3, there is a general increase in the proportion of mafic minerals (olivine and clinopyroxene) at the expense of plagioclase in the final mush. In Scenario 2, the clinopyroxene undersaturated nature of the initial melt phases leads to an increase in the proportion of plagioclase in the mush system.

Range of input and output values

Below, we show histograms for all three scenarios modelled in this study that demonstrate the range of input variables (in blue) and outputted crystallisation proportions (in red; Figs. 4, 5), 6).

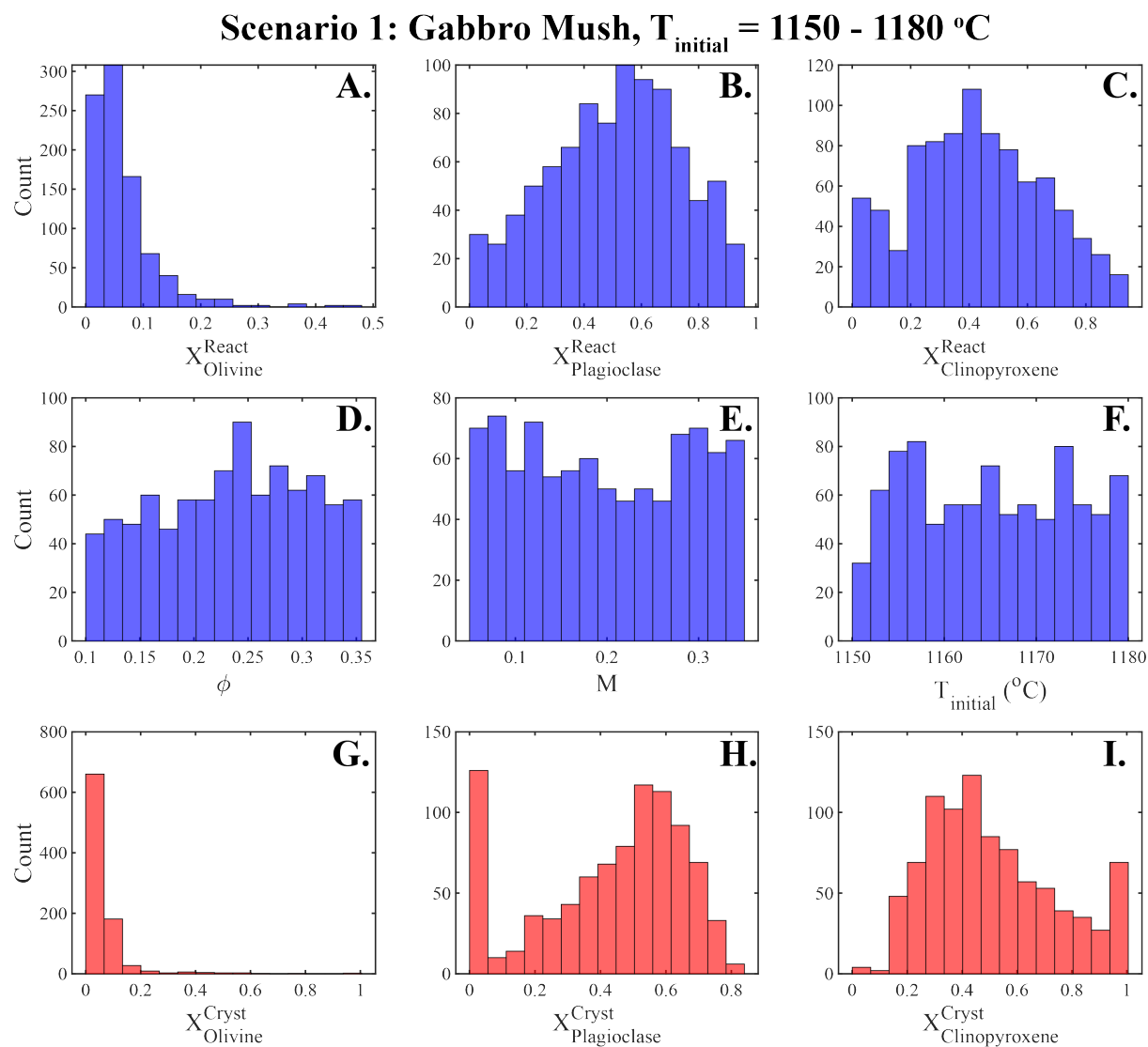


Figure 4: **A. - F.** demonstrate the range of input values used in the 450 simulations (each including 2 steps of melt-mush reaction) displayed in Fig. 3a-c of the main text. **G. - I.** demonstrates the crystallised mineral proportions for these simulations.

Scenario 2: Gabbro Mush, $T_{\text{initial}} = 1200 - 1230$ °C

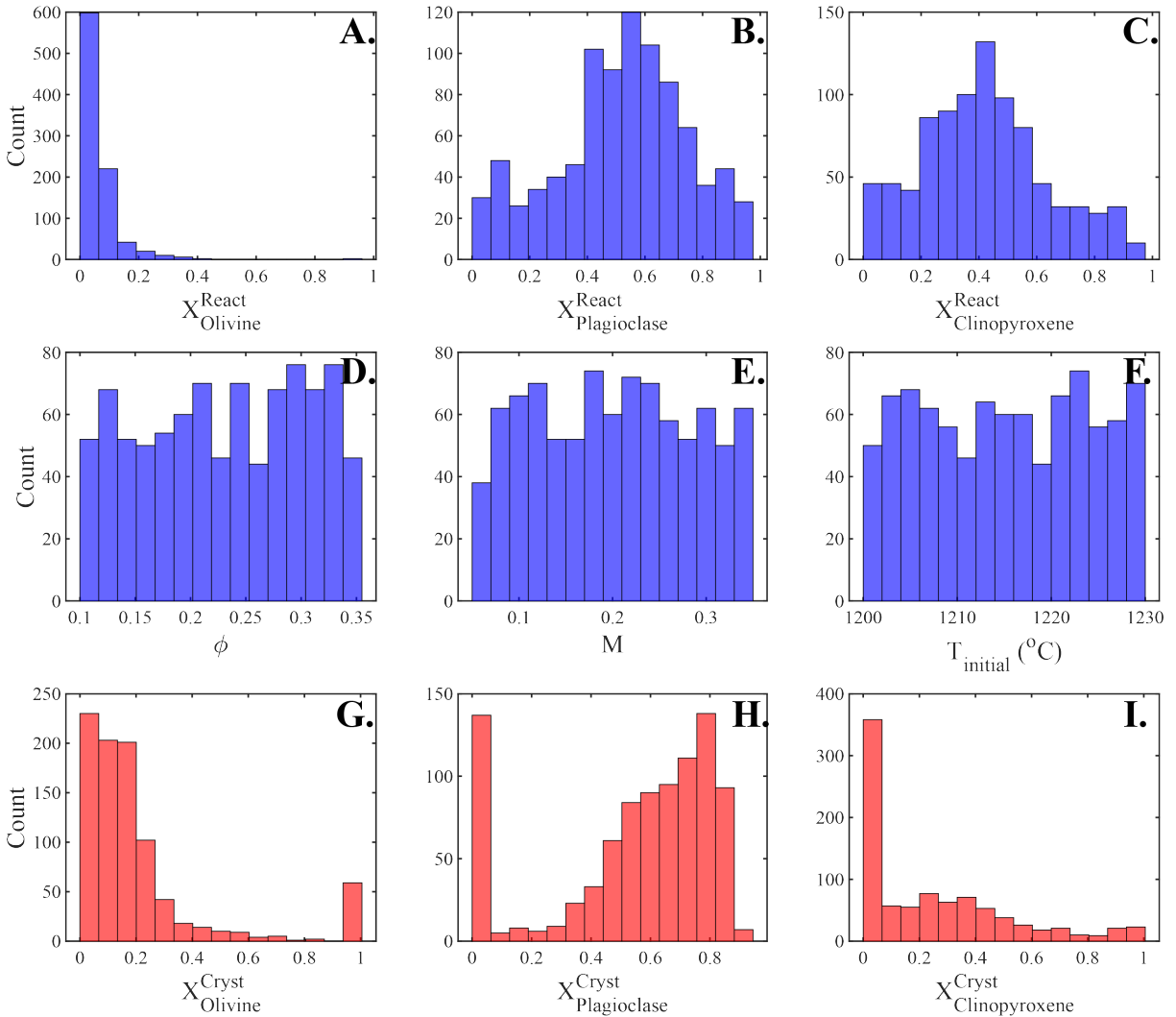


Figure 5: **A. - F.** demonstrate the range of input values used in the 450 simulations (each including 2 steps of melt-mush reaction) displayed in Fig. 3d-f of the main text. **G. - I.** demonstrates the crystallised mineral proportions for these simulations. Notably, compared to Fig. 4, a larger proportion of models show $X_{\text{Clinopyroxene}}^{\text{C}}$ values < 0.2 and $X_{\text{Plagioclase}}^{\text{C}}$ values > 0.6 .

Scenario 3: Troctolite Mush, $T_{\text{initial}} = 1150 - 1230 \text{ }^{\circ}\text{C}$

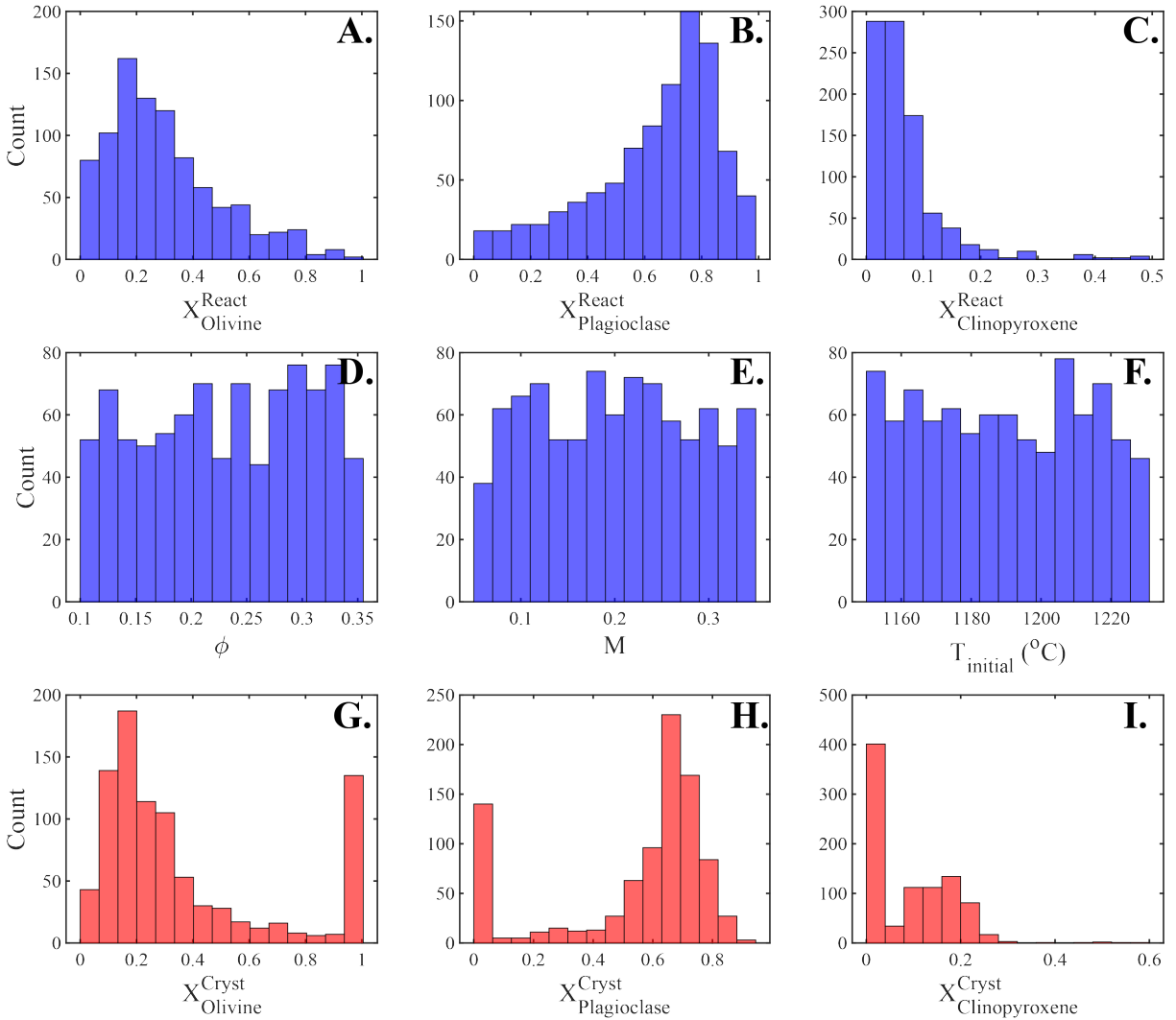


Figure 6: **A. - F.** demonstrate the range of input values used in the 450 simulations (each including 2 steps of melt-mush reaction) displayed in Fig. 3g-i of the main text. **G. - I.** demonstrates the crystallised mineral proportions for these simulations.

Testing different starting compositions

The starting composition used in this study, which is based on the composition of MgO-rich basalts from the South-West Indian Ridge (SWIR) in the compilation of Gale et al. (2013), was chosen for several reasons. First, it represents a reasonable estimate of primary magma compositions beneath the SWIR without having to apply a fractional crystallisation correction. Second, the fractional crystallisation models starting at this proposed primary melt composition provide a good match to the major element data of SWIR basalts, and thus the starting points for our reactive flow/melt-mush reaction models (which are taken from this fractional crystallisation model) are likely appropriate to the SWIR magmas.

Nevertheless, the choice of starting composition could, potentially, have an influence on our model results. To examine this possibility we re-ran all Scenario 1 & 3 models with the melt starting composition set to that of the most primitive Fracture Zone basalt from Dick et al. (2000). Models were not re-run for Scenario 2 as the liquidus temperature of this basalt at the pressure of the models (100 MPa) is only $\sim 1205^\circ\text{C}$. Additionally, only Scenario 3 models with a starting temperature below this liquidus temperature were used in the following figures. Overall, we can see that the choice of starting composition has very little influence on the results of our models (Figs. 7, 8, & 9).

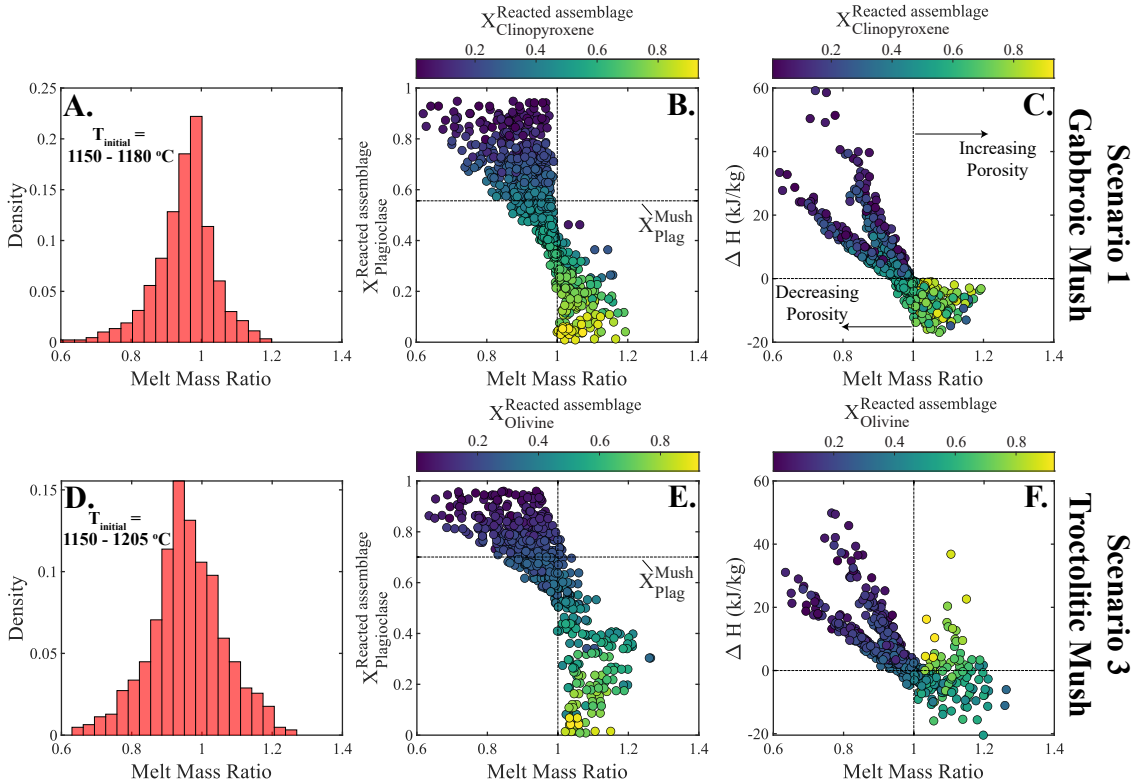


Figure 7: Melt-mush reaction model results for calculations using a starting melt composition from Dick et al. (2000). Scenario 1 & 3 models are shown, and display very similar results to Fig. 3 of the main text.

Scenario 1: Gabbro Mush, $T_{\text{initial}} = 1150 - 1180 \text{ }^{\circ}\text{C}$

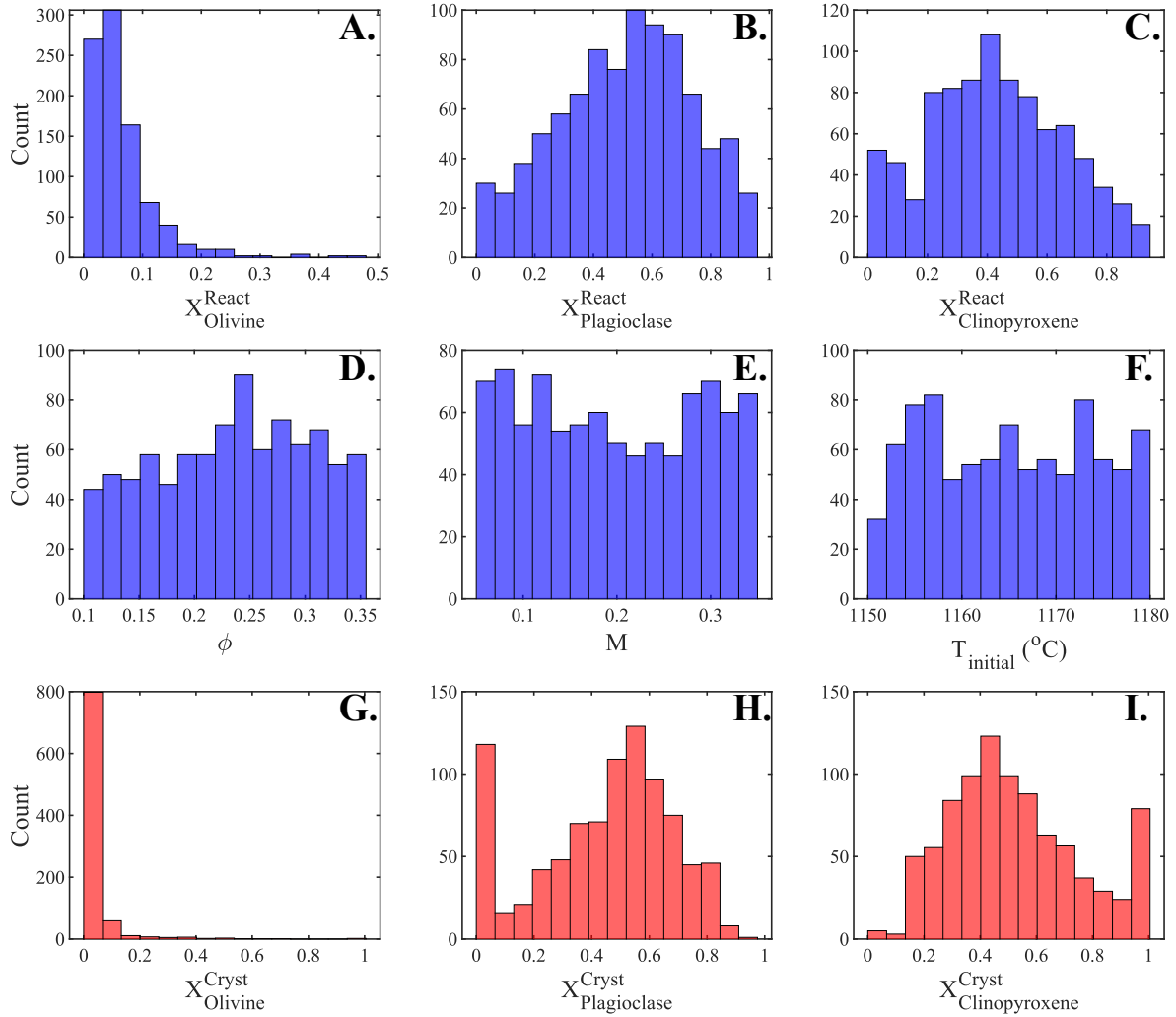


Figure 8: **A. - F.** demonstrate the range of input values used in the 450 simulations (each including 2 steps of melt-mush reaction) displayed in Fig. 7 panels **A. - C.**. **G. - I.** demonstrates the crystallised mineral proportions for these simulations.

Scenario 3: Troctolite Mush, $T_{\text{initial}} = 1150 - 1205 \text{ }^{\circ}\text{C}$

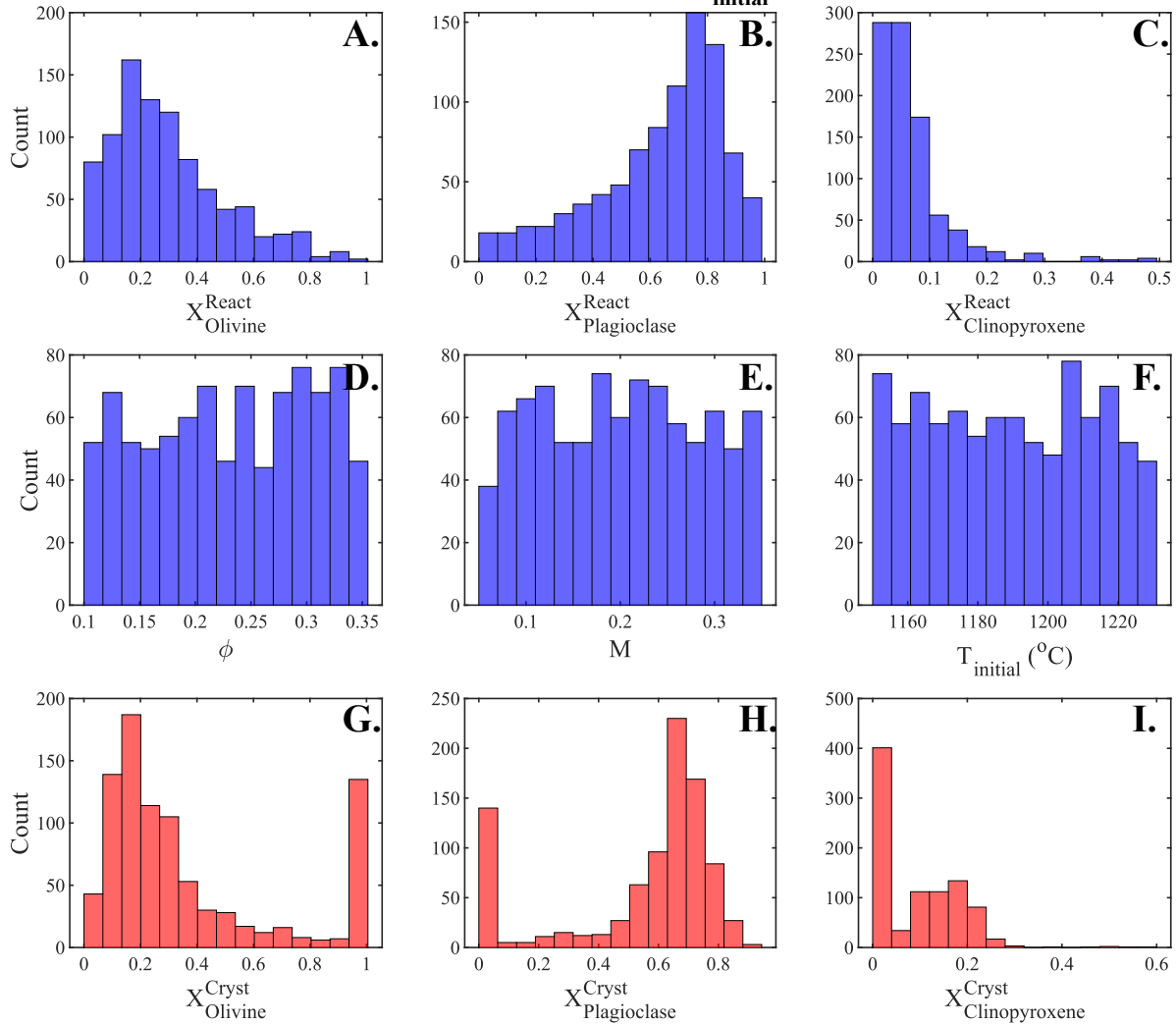


Figure 9: **A. - F.** demonstrate the range of input values used in the 450 simulations (each including 2 steps of melt-mush reaction) displayed in Fig. 7 panels **D. - F.** **G. - I.** demonstrates the crystallised mineral proportions for these simulations.

References

- Dick, H.J., Natland, J.H., Alt, J.C., Bach, W., Bideau, D., Gee, J.S., Haggas, S., Hertogen, J.G., Hirth, G., Holm, P.M. and Ildefonse, B., 2000. A long in situ section of the lower ocean crust: results of ODP Leg 176 drilling at the Southwest Indian Ridge. *Earth and planetary science letters*, 179(1), pp.31-51.
- Gale, A., Dalton, C.A., Langmuir, C.H., Su, Y. and Schilling, J.G., 2013. The mean composition of ocean ridge basalts. *Geochemistry, Geophysics, Geosystems*, 14(3), pp.489-518.
- Lissenberg, C.J. and MacLeod, C.J., 2016. A reactive porous flow control on mid-ocean ridge magmatic evolution. *Journal of Petrology*, 57(11-12), pp.2195-2220.